

## Modelling of heat transfer and pressure drop during flow boiling of CO<sub>2</sub> in a horizontal tube with periodic open cellular inserts

Jonas Bender, Konrad Dubil, Franz Korn, Thomas Wetzels, Benjamin Dietrich\*

*Institute of Thermal Process Engineering, Karlsruhe Institute of Technology (KIT), Kaiserstrasse 12, Karlsruhe 76131, Germany*

### ARTICLE INFO

#### Keywords:

Flow boiling  
Pressure drop  
Convective boiling heat transfer  
Nucleate boiling heat transfer  
Periodic open cellular structures  
POCS

### ABSTRACT

During flow boiling in horizontal tubes, highly porous inserts can improve the wetting of the tube wall and the convective boiling. The literature focuses on solid sponge structures with irregular cell geometries. Hence, in this work the local heat transfer and pressure drop during flow boiling of CO<sub>2</sub> in periodic open cellular structures with cubic and Kelvin cell geometry were investigated. A strong influence of the cell geometry on the heat transfer and pressure drop was found. By combining the Forchheimer term with a two-phase flow method (homogeneous model, drift flux model) a new pressure drop model is proposed. The model has a mean absolute percentage error (MAPE) of 12 %. Regarding the heat transfer, high-speed video recordings and an evaluation of the local heat transfer were used to test the tube segments for complete wetting. Thereafter, the convective boiling contribution was extracted from the local data of completely wetted tube segments by subtracting the nucleate boiling contribution. A separate model of the convective boiling is proposed for each cell type. The models have a MAPE of 20 %. Finally, the circumferentially averaged heat transfer coefficient was found to follow a superposition of the heat transfer of the liquid and vapor phase.

### 1. Introduction

In the literature on flow boiling in horizontal empty tubes, a strong dependence of the heat transfer on the prevailing flow pattern and thus on the wetting of the tube wall is reported [1–5]. In this regard, highly porous inserts such as solid sponges (often referred to as open-cell foams) or wire structures with a continuous solid and fluid phase are of great interest as they manipulate the flow patterns. Thereby, porous inserts were found to improve both the wetting of the tube wall [6,7], the convective boiling heat transfer and the convective heat transfer of the vapor phase [6,8–10]. In general, two designs of the inserts are distinguished. The inserts can be materially bonded to the tube wall or installed via clearance fits. The first design offers an additional increase in the heat transfer surface. The second design, which this contribution focusses on, offers a high modularity, whereby changes in the heat transfer surface are negligible due to high contact resistances.

A relatively new class of porous inserts are periodic open cellular structures (POCS). Thereby, the additive manufacturing process of POCS from various metal alloys, ceramics or polymers [11,12] offers an immense variety in the design of their respective cell geometry and their area of application [13–17]. For single-phase flows, numerous works

exist which investigate the thermal and hydrodynamic processes in POCS at various flow regimes [14–18]. For two-phase flows with POCS, some investigations on the hydrodynamics have been conducted [19–21], whereas no studies on flow boiling exist to the authors' knowledge.

Hence, in this work the pressure drop and heat transfer during flow boiling with different POCS (cubic cells (cu), Kelvin cells (kel)) are examined. Regarding the modelling of the measurement data a promising starting point is provided by the models for solid sponge structures of Weise et al. [6,22]. Thereby, established single-phase models are combined with suitable two-phase flow methods (homogeneous model, drift flux model) to account for slip between the phases.

Regarding the refrigerant, CO<sub>2</sub> was selected, as it has a low global warming potential and does not contribute to ozone depletion, unlike many synthetic refrigerants such as chlorofluorocarbons. Furthermore, it is abundantly available as a byproduct of various industrial processes and due to its non-toxicity and non-flammability preferred in applications with high safety concerns [23].

Against this background, this contribution focusses first in chapter 2 on the theoretical basis of two-phase flow methods, followed by the state of the art of pressure drop and heat transfer modelling during flow boiling with porous inserts. In chapter 3, the experimental setup and the

\* Corresponding author.

E-mail address: [benjamin.dietrich@kit.edu](mailto:benjamin.dietrich@kit.edu) (B. Dietrich).

**Nomenclature***Latin symbols*

|             |                                                             |
|-------------|-------------------------------------------------------------|
| $A_0$       | cross-sectional area of the empty tube / $m^2$              |
| $A_c, A_f$  | projected cross-sectional areas of one cell / $m^2$         |
| $A_j$       | curved surface area of one segment / $m^2$                  |
| $a$         | variable for target values                                  |
| $C_0$       | distribution factor / –                                     |
| $c_p$       | isobaric specific heat capacity / $J\ kg^{-1}\ K^{-1}$      |
| $c_v$       | isochoric specific heat capacity / $J\ kg^{-1}\ K^{-1}$     |
| $d$         | diameter / m                                                |
| $f_{dry}$   | dry fraction / –                                            |
| $g$         | gravitational acceleration / $m\ s^{-2}$                    |
| $H$         | specific enthalpy / $J\ kg^{-1}$                            |
| $h$         | heat transfer coefficient / $W\ m^{-2}\ K^{-1}$             |
| $K$         | dissipation factor / –                                      |
| $k$         | thermal conductivity / $W\ m^{-1}\ K^{-1}$                  |
| $k_p$       | coverage factor / –                                         |
| $kA$        | thermal transmittance / $W\ K^{-1}$                         |
| $l$         | length / m                                                  |
| $\tilde{M}$ | molar mass / $kg\ mol^{-1}$                                 |
| $\dot{M}$   | mass flow / $kg\ s^{-1}$                                    |
| $m$         | mass / kg                                                   |
| $\dot{m}$   | mass flux / $kg\ m^{-2}\ s^{-1}$                            |
| $n$         | number of tube segments / –                                 |
| $N$         | number of data points / –                                   |
| $P$         | power / W                                                   |
| $p$         | system pressure / saturation pressure / $N\ m^{-2}$         |
| $\dot{Q}$   | heat transfer rate / W                                      |
| $\dot{q}$   | heat flux / $W\ m^{-2}$                                     |
| $S_v$       | specific surface area regarding the total volume / $m^{-1}$ |
| $T$         | temperature / K                                             |
| $u$         | velocity / $m\ s^{-1}$                                      |
| $u_e$       | expanded uncertainty                                        |
| $V$         | volume / $m^3$                                              |
| $\dot{V}$   | volumetric flow rate / $m^3\ s^{-1}$                        |
| $\dot{x}$   | vapor quality / –                                           |
| $z$         | horizontal distance / m                                     |

*Dimensionless groups*

|      |                             |
|------|-----------------------------|
| $a$  | dimensionless strut length  |
| $E$  | dimensionless length scales |
| $Ma$ | Mach number                 |
| $Nu$ | Nusselt number              |
| $Pe$ | Péclet number               |
| $Pr$ | Prandtl number              |
| $Re$ | Reynolds number             |

*Greek symbols*

|                 |                                                             |
|-----------------|-------------------------------------------------------------|
| $\beta$         | Forchheimer coefficient / $m^{-1}$                          |
| $\gamma$        | angle of inclination / –                                    |
| $\Delta H_{LV}$ | specific enthalpy of evaporation / $J\ kg^{-1}$             |
| $\Delta p$      | pressure drop / $N\ m^{-2}$                                 |
| $\Delta z$      | unit length / horizontal distance between two points / m    |
| $\varepsilon$   | void fraction / –                                           |
| $\eta$          | dynamic viscosity / Pa s                                    |
| $\theta_{dry}$  | dry angle of tube / –                                       |
| $\theta_j$      | angle of one tube segment / –                               |
| $\rho$          | density / $kg\ m^{-3}$                                      |
| $\sigma$        | surface tension / $N\ m^{-1}$                               |
| $\sigma_s$      | standard deviation of a pixel, normalized to gray scale / – |

|          |                                 |
|----------|---------------------------------|
| $\tau$   | tortuosity / –                  |
| $\tau_w$ | wall shear stress / $N\ m^{-2}$ |
| $\psi$   | porosity / –                    |

*Sub-/superscripts*

|        |                                                 |
|--------|-------------------------------------------------|
| 0      | referring to the empty tube                     |
| 1      | referring to first measurement                  |
| 2      | referring to repeated measurement               |
| A      | referring to area                               |
| a      | referring to annular                            |
| acc    | referring to acceleration                       |
| CAD    | referring to computer aided design              |
| c      | referring to critical                           |
| cb     | convective boiling                              |
| cu     | referring to cubic cells                        |
| D      | referring to drift                              |
| el     | referring to electrical                         |
| exp    | referring to experimental                       |
| F      | referring to fluid                              |
| h      | referring to homogeneous                        |
| heated | referring to heated region                      |
| i      | referring to the inside of the tube / tube wall |
| in     | referring to inaccessible / inside              |
| inl    | referring to inlet of pre-evaporator            |
| ins    | referring to insulation                         |
| $j$    | counter variable                                |
| $k$    | counter variable                                |
| kel    | referring to Kelvin cells                       |
| L      | referring to liquid                             |
| m      | referring to the momentum                       |
| mod    | referring to modelled                           |
| nb     | nucleate boiling                                |
| n-cu   | referring to tilted cubic cells                 |
| o      | referring to open                               |
| out    | referring to outside                            |
| p      | referring to equivalent particle                |
| pm     | referring to plane of measurement               |
| par    | referring to parasitic                          |
| pt     | referring to pressure tap                       |
| S      | referring to mixture                            |
| s      | referring to strut                              |
| sat    | referring to saturation                         |
| st     | referring to stratified                         |
| solid  | referring to the solid phase                    |
| sp     | referring to single-phase                       |
| spo    | referring to sponge                             |
| struct | referring to the entire cylindrical structure   |
| tp     | referring to two-phase                          |
| ts     | referring to test section                       |
| V      | referring to vapor                              |
| w      | referring to window                             |

*Abbreviation*

|      |                                        |
|------|----------------------------------------|
| APE  | absolute percentage error              |
| CAD  | computer aided design                  |
| CT   | computed tomography                    |
| fps  | frames per second                      |
| MAPE | mean absolute percentage error         |
| MAPR | mean absolute percentage repeatability |
| PEEK | polyether ether ketone                 |
| POCS | periodic open cellular structures      |
| STL  | stereolithography                      |
| TC   | thermocouple                           |

functioning of the measurement concept are presented, including an uncertainty analysis of the relevant target values as well as an overview of the investigated POCS. Finally, in chapter 4, the measurement data is compared with the existing pressure drop and heat transfer models of porous inserts with irregular cell geometries, followed by an evaluation of new models considering the regular cell geometry of POCS.

## 2. Model approaches

### 2.1. Two-phase flow methods

To determine the heat transfer and pressure drop of two-phase flows, knowledge of the average or local flow velocities of the phases is required. Various methods for determining the phase velocities ( $u_L$ ,  $u_V$ ) exist, which are categorized into models with and without slip between the phases. Woldesemayat [24] presents a comprehensive review of different two-phase flow methods. The chosen method affects the momentum density  $\rho_m$ , which is used to model the two-phase flow as a whole. The momentum density (see Eq. (1)) is derived from the one-dimensional momentum equation of a two-phase flow by means of a vapor quality weighted combination of the phase velocities ( $u_m = (1 - \dot{x}) \cdot u_L + \dot{x} \cdot u_V$ ) [25]. Here  $\dot{x}$  corresponds to the vapor quality,  $\varepsilon$  to the void fraction and  $\rho_L$ ,  $\rho_V$  to the liquid and vapor density.

$$\rho_m = \left( \frac{(1 - \dot{x})^2}{\rho_L \cdot (1 - \varepsilon)} + \frac{\dot{x}^2}{\rho_V \cdot \varepsilon} \right)^{-1} \quad (1)$$

In the following, the basics of two-phase flow methods (homogeneous model, drift flux model) and their effects on the momentum density are presented.

#### Homogeneous model:

In the homogeneous model, no slip occurs between the phases, therefore the liquid and vapor velocity are identical ( $u_m = u_L = u_V$ ). Consequently, the void fraction  $\varepsilon_h$  is obtained by Eq. (2).

$$\varepsilon = \varepsilon_h = \left( 1 + \frac{(1 - \dot{x}) \cdot \rho_V}{\dot{x} \cdot \rho_L} \right)^{-1} \quad (2)$$

Through a combination of Eq. (2) with (Eq. (1)) the homogeneous density  $\rho_h$  is derived.

$$\rho_h \equiv \rho_m = \left( \frac{(1 - \dot{x})}{\rho_L} + \frac{\dot{x}}{\rho_V} \right)^{-1} \quad (3)$$

The homogeneous model is particularly suitable for two-phase flows with pronounced momentum exchange between the phases.

#### Drift flux model:

The drift flux model treats the two-phase flow as a pseudo fluid with slip between the phases [26]. Thereby, an empirical parameter as for example the drift velocity of the vapor phase  $u_{VD}$  is required, to account for the slip. The drift velocity corresponds to the velocity difference between the vapor velocity  $u_V$  and the superficial mixture velocity  $u_{S0}$  multiplied by the distribution factor  $C_0$  [27]. Numerous variations of the drift flux model exist [24], whereby for flow boiling in horizontal tubes with and without porous inserts [1,2,6–8,28], the model of Rouhani [29] is widely adopted. Here, the vapor velocity  $u_V$  is given by Eq. (4). The mass flux in the empty tube is  $\dot{m}_0$  and the surface tension  $\sigma$ .

$$u_V = C_0 \cdot u_{S0} + u_{VD} = [1 + 0.12 \cdot (1 - \dot{x})] \cdot \left[ \frac{(1 - \dot{x})}{\rho_L} + \frac{\dot{x}}{\rho_V} \right] \cdot \dot{m}_0 + 1.18 \cdot (1 - \dot{x}) \left[ \frac{\sigma \cdot g \cdot (\rho_L - \rho_V)}{\rho_L^2} \right]^{0.25} \quad (4)$$

Subsequently, the void fraction  $\varepsilon_D$  is obtained by Eq. (5).

$$\varepsilon = \varepsilon_D = \frac{\dot{m}_0 \cdot \dot{x}}{u_V \cdot \rho_V} \quad (5)$$

In this case, the momentum density corresponds to the momentum

density of the pseudo fluid (see Eq. (1)). The drift flux model is suitable for two-phase flows with reduced momentum exchange between the phases.

### 2.2. Pressure drop

#### State of the art:

In case of two-phase flows through empty tubes, typically the one-dimensional mass and momentum conservation equations of an infinitesimal volume element represent the theoretical basis for modelling the pressure drop. The expression of the pressure gradient shown in Eq. (6) can be derived as the sum of three components, based on shear stresses, gravitational forces and acceleration effects. Here,  $d_i$  stands for the inner diameter of the tube,  $\tau_w$  for the wall shear stress,  $g$  for the gravitational acceleration and  $\gamma$  for the angle of inclination of the tube.

$$\left( \frac{dp}{dz} \right)_{tp,0} = -\frac{4 \cdot \tau_w}{d_i} - ((1 - \varepsilon) \cdot \rho_L + \varepsilon \cdot \rho_V) \cdot g \cdot \sin(\gamma) - \dot{m}_0^2 \cdot \frac{d}{dz} \left( \frac{1}{\rho_m} \right) \quad (6)$$

However, for horizontal tubes ( $\gamma = 0$ ), the gravitational component is omitted. Furthermore, Weise et al. [22] approximated the acceleration component due to evaporation (see Appendix B) of the data of two-phase flows through tubes with metal sponges (spo) [7,8,22,30] to be at least two orders of magnitude smaller than the total pressure drop. Thereby, the authors identified shear stresses as the main cause of the pressure drop. As a result, Weise et al. [22] proposed a new model for the pressure drop per unit length  $(\Delta p / \Delta z)_{tp,spo}$  for two-phase flows through metal sponges (see Eq. (7)). It results from a combination of the homogeneous model (see Section 2.1) with the Forchheimer equation for single-phase flows from [31,32], neglecting the impact of the Darcy term.

$$-\left( \frac{\Delta p}{\Delta z} \right)_{tp,spo} = \frac{\beta}{\rho_m} \cdot \dot{m}_0^2 = \frac{\beta}{\rho_h} \cdot \dot{m}_0^2 \quad (7)$$

For the calculation of the Forchheimer coefficient  $\beta$  the work of Inayat et al. [33] is recommended (see Eq. (8)). Although their expression of the tortuosity  $\tau$  (see Eq. (9)) was derived for sponges, the underlying model idea can be transferred to Kelvin and cubic cells as well. Here,  $S_v$  corresponds to specific surface area with regard to the total volume and  $d_w$  and  $\psi_o$  are the average window diameter and the open porosity (see Section 3.2).

$$\beta = \frac{\tau^3 \cdot S_v}{2 \cdot 4 \cdot \psi_o^3} \quad (8)$$

$$\tau = 1 + \frac{d_w \cdot S_v}{4 \cdot \psi_o} \quad (9)$$

#### Alternative model approach:

Due to the large morphological differences between POCS and the irregular cell structures of sponges, an alternative modeling approach is introduced in this work.

A suitable starting point for the model development is presented by the work of Klumpp et al. [15], who investigated the pressure drop of air flows in POCS with cubic and tilted cubic cells (n-cu). They found the pressure drop to be dominated by inertial forces at equivalent particle Reynolds numbers  $Re_p > 120$  (see Appendix B). The corresponding pressure drop model is shown in Eq. (10). The model contains only geometric parameters. At identical open porosity, the Forchheimer coefficient of tilted cubic cells  $\beta_{n-cu}$  equals the product of the Forchheimer coefficient of cubic cells  $\beta_{cu}$  and a quotient based on the area-related porosities of the respective tilted and cubic cells ( $1 - \psi_{A,n-cu}$ ,  $1 - \psi_{A,cu}$ ). The area-related porosity  $\psi_{A,j}$  equals the quotient of the projected free cross-sectional area  $A_{f,j}$  and the total cross-sectional area  $A_{c,j}$  of one cell.

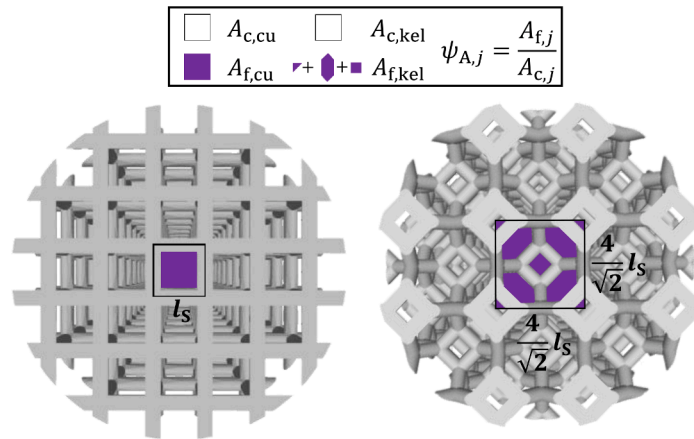


Fig. 1. Area-related porosity  $\psi_{A,j} = A_{f,j}/A_{c,j}$  of the investigated structures with cu (left) and kel (right).

$$\begin{aligned} -\left(\frac{\Delta p}{\Delta z}\right)_{sp,POCS} &= \frac{\psi_{A,cu}}{(1-\psi_{A,cu})} \cdot \frac{(1-\psi_o)}{\psi_o} \cdot \frac{(1-\psi_{A,n-cu})}{(1-\psi_{A,cu})} \cdot \frac{S_v \cdot \rho_F}{\psi_o^3} \cdot u_0^2 \\ &= \beta_{cu} \cdot \frac{(1-\psi_{A,n-cu})}{(1-\psi_{A,cu})} \cdot \rho_F \cdot u_0^2 = \beta_{n-cu} \cdot \rho_F \cdot u_0^2 \end{aligned} \quad (10)$$

In the following, the above model is extended to the geometry of Kelvin cells and combined with a two-phase flow method (see Section 2.1). The variation of the cell type is treated analogously to the tilting of cubic cells, whereby a change of the cell type leads to a variation of the area-related porosity (see Fig. 1). All required equations are included in Appendix A.

Under consideration of the above modifications, the final two-phase pressure drop equation is shown in Eq. (11). For cubic cells ( $j = cu$ ), the quotient based on the area-related porosities is 1.

$$-\left(\frac{\Delta p}{\Delta z}\right)_{tp,POCS} = \frac{\psi_{A,cu}}{(1-\psi_{A,cu})} \cdot \frac{(1-\psi_o)}{\psi_o} \cdot \frac{(1-\psi_{A,j})}{(1-\psi_{A,cu})} \cdot \frac{S_{v,j} \cdot \dot{m}_0^2}{\psi_o^3 \cdot \rho_m} = \beta_j \cdot \frac{\dot{m}_0^2}{\rho_m} \quad (11)$$

From the content of this section the following hypothesis is formulated:

- The pressure drop of two-phase flows in POCS can be modelled in accordance to solid sponges by combining the homogeneous model with a single-phase model for the Forchheimer term.

### 2.3. Heat transfer

#### State of the art:

Depending on the operating conditions, the flow boiling heat transfer in horizontal tubes with porous inserts is influenced by several processes: nucleate boiling heat transfer, convective boiling heat transfer, wetting of the tube wall and consequently also the convective heat transfer of the vapor phase. If the structures are inserted via clearance fits, no changes to the nucleate boiling contribution are observed compared to empty tubes [6]. Thereby, porous inserts are found to affect mainly the latter three processes [6,8].

For solid sponge inserts, Weise et al. [6] found that the circumferentially averaged heat transfer coefficient  $h_{tp}$  at the tube wall (see Eq. (12)) can be described as a superposition of the heat transfer of the liquid and vapor phase ( $h_L, h_V$ ), as it was first reported for empty tubes by Kattan et al. [2]. Here,  $f_{dry,j}$ ,  $h_{nb}(\dot{q}_{i,j})$ ,  $h_{cb,j}$ ,  $h_{v,j}$  correspond to the dry fraction of the tube segment  $j$ , the nucleate boiling heat transfer

coefficient at the local heat flux  $\dot{q}_{i,j}$ , the convective boiling heat transfer coefficient and the convective heat transfer coefficient of the vapor phase. The total number of tube segments (see Section 3.1) is  $n$ .

$$h_{tp} = \frac{1}{n} \sum_{j=1}^n \left[ f_{dry,j} \cdot h_{v,j} + (1-f_{dry,j}) \cdot \sqrt[3]{h_{nb}^3(\dot{q}_{i,j}) + h_{cb,j}^3} \right] \quad (12)$$

The dry fraction is defined by Eq. (13) as the ratio of the dry angle  $\theta_{dry,j}$  of one tube segment and the total angle of one tube segment  $\theta_j$ .

$$f_{dry,j} = \frac{\theta_{dry,j}}{\theta_j} \quad (13)$$

The dry angle depends on the prevailing flow pattern, which is influenced by the geometry of the porous inserts [6] (see Appendix C).

For solid sponges, Weise et al. [6] used the single-phase model of Bianchi et al. [34] to calculate both the convective boiling heat transfer coefficient ( $h_{cb,j}$ ) and the convective heat transfer coefficient of the vapor phase ( $h_{v,j}$ ) (see Eq. (12)). The model is depicted in Eq. (14). The window diameter  $d_w$  corresponds to the characteristic length scale and  $k$  to the thermal conductivity of the fluid. The Péclet number  $Pe$  is defined as the product of Reynolds and Prandtl number ( $Re, Pr$ ).

$$Nu_{cb/v} = \frac{h_{cb/v} \cdot d_w}{k_{L/v}} = 1.97 + 0.09 \cdot (Pe_{L/v})^{0.73}; Pe_{L/v} = Re_{L/v} \cdot Pr_{L/v} \quad (14)$$

For two-phase flows, the expression of the Reynolds number was modified (Eqs. (15), (16)). The void fraction  $\varepsilon$  is calculated according to the respective two-phase flow method (see Section 2.1). Weise et al. [6] found the convective boiling/convective heat transfer in the upper half of tube to follow the homogeneous and in the lower half of the tube to follow the drift flux model by Rouhani [29].

$$Re_L = \frac{\dot{m}_0 \cdot (1-\dot{x}) \cdot d_w}{\psi_o \cdot \eta_L \cdot (1-\varepsilon)} \quad (15)$$

$$Re_V = \frac{\dot{m}_0 \cdot \dot{x} \cdot d_w}{\psi_o \cdot \eta_V \cdot \varepsilon} \quad (16)$$

Regarding the nucleate boiling heat transfer coefficient  $h_{nb}(\dot{q}_i)$ , numerous works from literature [1–3,6,8] have found the model of Cooper [35] shown in Eq. (17) to describe the measurement data for empty tubes and tubes with solid sponge inserts best. Here,  $p_c$  corresponds to the critical pressure and  $\bar{M}$  to the molar mass of the fluid.

$$\frac{h_{nb}(\dot{q}_i)}{(\text{W m}^{-2} \text{K}^{-1})} = 55 \cdot \left(\frac{p}{p_c}\right)^{0.12} \cdot \left[-\log_{10}\left(\frac{p}{p_c}\right)\right]^{-0.55} \cdot \left(\frac{\tilde{M}}{\text{g mol}^{-1}}\right)^{-0.5} \cdot \left(\frac{\dot{q}_i}{\text{W m}^{-2}}\right)^{0.67} \quad (17)$$

From the content of this section the following three hypotheses are formulated:

- In analogy to solid sponges, the convective boiling heat transfer in POCS can be described by the model of Bianchi et al. [34].
- The convective boiling heat transfer in the upper and lower half of the tube follows the homogeneous and drift flux model, respectively.
- The circumferentially averaged heat transfer can be described by a superposition of the heat transfer of the liquid and vapor phase (see Eq. (12)).

### 3. Materials and methods

#### 3.1. Experimental setup and measurement concept

In the following, the experimental setup of the horizontal test section (ts) and the functioning of the measurement concept to determine the two target values (pressure drop per unit length and local heat transfer coefficient) are presented. The determination of the vapor quality is included in Appendix C. For a detailed description of the entire experimental setup (fluid loop and test section) the reader is referred to the Ph.D. thesis of Haertlé born Weise [36].

Fig. 2 shows a longitudinal section of the test section including the sight glass (top) as well as a cross section of the first plane of

measurement pm1 (bottom) with an exemplary POCS (kel). The sight glass serves as an optical access to determine the flow patterns and the wetting of the tube wall (see Section 4.2.1) by a high-speed camera (Motion corder analyzer SR-500c, KODAK). Thereby, the CO<sub>2</sub> enters the test section in saturated state with a vapor quality set by pre-evaporators.

The pressure drop  $\Delta p$  along the test section is measured using a differential pressure transducer (3051 Rosemount, EMERSON) connected to a pressure tap at the inlet and outlet of the test section.

The pressure drop per unit length is then calculated using Eq. (18) as the ratio of the pressure drop and the distance between the pressure taps  $l_{pt}$ .

$$\frac{\Delta p}{\Delta z} = \frac{\Delta p}{l_{pt}} \quad (18)$$

The tube of the test section is made from brass and has an inner diameter  $d_i$  of 14 mm. The test section is subdivided along its circumference into six equally sized segments (see Fig. 6, bottom). The segments are separated by grooves (see Fig. 2) to reduce azimuthal heat conduction. Over its length, the test section has three planes of measurements (pm). Each pm contains six thermocouples (TC, type K class 1 IEC 584-3. ELECTRONIC SENSOR), which are soldered into the tube wall in 60° steps. In the context of this work, only the measurement results of pm1 are presented, since in accordance to the work of Weise

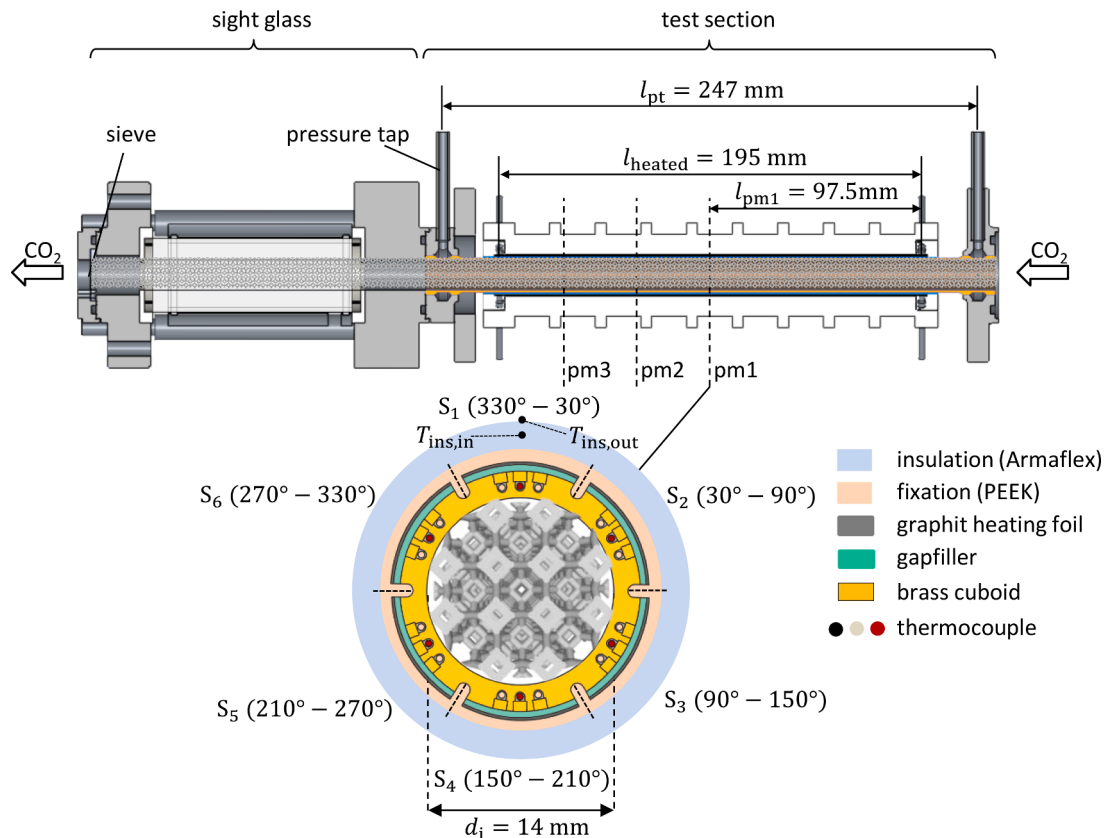


Fig. 2. Longitudinal view of the test section and sight glass (top) and cross-section of pm1 (bottom) with kel inserts. The thermocouples of pm1 are depicted in red. Depiction was modified from Weise et al. [37] (licensed under CC BY-NC 4.0 DEED).

et al. [6], no relevant differences between the different planes of measurement were found.

During a measurement each segment is individually heated by a graphite heating foil (SIGRAFLEX® F02012TH, SGL CARBON). The electrical power consumed by the heating foils is measured with digital power meters (WT1030, YOKOGAWA). By adjustment of the power input, all measurements are conducted with a constant inner wall temperature (first-type boundary condition). A constant wall temperature is assumed if the temperature reading of each thermocouple in a pm is within the expanded uncertainty ( $u_e(T) = 0.3$  K) according to GUM [38] of type B. Furthermore, the influence of inhomogeneities of the wall temperature was investigated with the simulation software Simcenter STAR-CCM+ (v.9.04.009) and accounted for in the uncertainty analysis (see Section 3.3). For a detailed description of the simulation routine the reader is referred to [36].

The local heat transfer coefficient  $h_{tp,k,j}$  of a plane of measurement  $k$  (pm1 - pm3) of a segment  $j$  ( $S_1$ - $S_6$ ) is determined with the kinetics of heat transfer using Eq. (19). Here,  $\dot{q}_{el,j}$  corresponds to the heat transfer rate of the individual segment generated by the associated heating foil. It is determined from the measured electrical power  $P_{el,j}$ , multiplied by a dissipation factor  $K$ , accounting for the power losses in the connection lines. The heat transfer rate  $\dot{q}_{par}$  corresponds to the parasitic heat input from the environment and is calculated from the thermal transmittance  $(kA)_{ins}$  and the temperature difference across the insulation  $(T_{ins,out} - T_{ins,in})$  of the test section. The heated surface  $A_j$  equals the curved surface area of one segment, wherein  $l_{heated}$  is the electrically heated length of the test section. The inner wall temperature  $T_{k,j}$  is extrapolated from the measurement data of the respective thermocouple assuming one-dimensional heat conduction in the tube wall. The saturation temperature  $T_{sat,k}(p_k)$  is determined from the saturation pressure  $p_k$  using the equation of state for CO<sub>2</sub> by Span and Wagner [39].

$$h_{tp,k,j} = \frac{\left(\dot{q}_{el,j} + \frac{\dot{q}_{par}}{6}\right)}{A_j(T_{i,k,j} - T_{sat,k}(p_k))} = \frac{\left(K \cdot P_{el,j} + \frac{(kA)_{ins}(T_{ins,out} - T_{ins,in})}{6}\right)}{\frac{\pi}{6} d_i \cdot l_{heated} \cdot (T_{i,k,j} - T_{sat,k}(p_k))} \quad (19)$$

The circumferentially averaged heat transfer coefficient  $h_{tp,k}$  is calculated from the local measurement data according to Eq. (20).

$$h_{tp,k} = \frac{1}{6} \sum_{j=1}^{n=6} h_{tp,k,j} \quad (20)$$

In the further course of this work, the local and circumferentially averaged heat transfer coefficients of pm1 are referred to as  $h_{tp,j}$  and  $h_{tp}$ .

As for the POCS, all investigated inserts (see Section 3.2) were manufactured in form of cylindrical segments and inserted into the test section as well as the sight glass with clearance fits of < 100  $\mu$ m.

Additionally, to avoid an influence of entrance effects like the formation of flow patterns or stagnation point flows on the measurement data, the investigated POCS were also installed upstream of the test section. Considering the results of Haertlé born Weise [36] for solid sponges, the structures were installed with a length of more than 30 cells upstream of the inlet pressure tap, ensuring an exclusion of entrance effects.

### 3.2. Periodic open cellular structures

Two types of periodic open cellular structures (POCS) with cubic and Kelvin cell geometry were investigated. The POCS were additively manufactured in cylindrical form with a mean diameter  $d_{struct}$  of approx. 13.9 mm and a mean length  $l_{struct}$  of approx. 51 mm. Both types of POCS are made of an aluminum alloy (AlSi10Mg). The cubic cell structures were manufactured by FKM Laser Sintering in, Biedenkopf, Germany and the Kelvin cell structures by citim, Barleben, Germany using the laser beam melting (SLM) process. In total, 11 samples of each cell type were produced. For both POCS, CT scans were performed using an area detector with a voxel size of 50  $\mu$ m<sup>3</sup>. Both the total surface area and the inaccessible pore volume were determined from the CT scans. Fig. 3 shows the CT scans of the investigated structures including their ideal window geometries.

The experimentally determined (exp) geometry parameters of the above structures as well as the respective nominal values from the computer-aided design (CAD) tools are given in Table 1. The strut length  $l_{s,exp}$  and diameter  $d_{s,exp}$  were determined from the stereolithography (STL) files of the CT scans by evaluating 20 struts per structure. The experimental open porosity  $\psi_{o,exp}$  was determined from the solid and bulk density of the structures, subtracting the inaccessible porosity (see Appendix A). The nominal open porosity  $\psi_{o,CAD}$ , the average window diameters  $d_{w,exp}$  and  $d_{w,CAD}$  and the nominal specific surface area  $S_{v,CAD}$  were determined using the equations of Horneber [40] (see Appendix

**Table 1**

Overview of the experimental and nominal values of all relevant geometry parameters of the cu and kel structures. The nominal values are depicted in brackets.

| Geometry parameter                    | cubic cells | Kelvin cells  |
|---------------------------------------|-------------|---------------|
| Strut diameter $d_s$ / mm             | 0.63 (0.64) | 0.63 (0.64)   |
| Strut length $l_s$ / mm               | 2.21 (2.18) | 1.27 (1.33)   |
| Average window diameter $d_w$ / mm    | 1.77 (1.73) | 1.33 (1.41)   |
| Open porosity $\psi_o$ / -            | 0.85 (0.83) | 0.81 (0.83)   |
| Inaccessible porosity $\psi_{in}$ / - | 0.0003 (0)  | 0.002 (0)     |
| Area related porosity $\psi_A$ / -    | 0.51 (0.5)  | 0.38 (0.39)   |
| Specific surface area $S_v$ / 1/m     | 919 (928.6) | 871.2 (870.1) |
| Tortuosity $\tau$ from Eq. (9) / -    | 1.48 (1.48) | 1.36 (1.37)   |

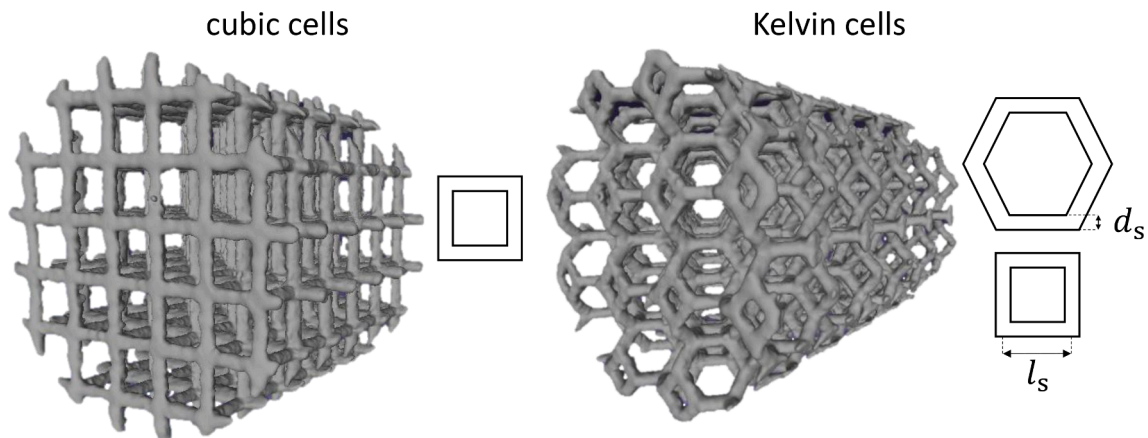


**Fig. 3.** CT scans and ideal window geometry of the investigated POCS consisting of cu (left) and kel (right).

A). Thereby, spheres with removed spherical calottes are used as nodes. The values of the specific surface area  $S_{v,exp}$  post manufacturing were extracted from the CT scans, subtracting the front and side surfaces of the structures. The area related porosity  $\psi_{A,exp}$  and  $\psi_{A,CAD}$  were determined according to Fig. 1.

A comparison between the experimental and nominal values shows that the geometry parameters predefined by the CAD are achieved with high accuracy by the additive manufacturing processes. Thereby, the maximum absolute percentage deviation between the nominal and experimental values is 5.7 %. Due to the good agreement, only the nominal values of both structures are considered for the pressure drop (see Section 4.1) and heat transfer modelling (see Section 4.2). The use of the nominal values has a decisive advantage as the pressure and heat transfer models can be directly integrated into the design process of POCS, omitting cost- and time-intensive structural characterization procedures.

### 3.3. Uncertainty analysis and repeatability of measurements

With the aim of quantifying the uncertainty of all target values, an uncertainty analysis according to GUM [38] of type B was carried out with a coverage factor  $k_p$  of 2. A detailed description of the respective uncertainty analysis including the standard uncertainties of all sensors is contained in the work of Weise et al. [6]. Hence, in this work only the uncertainties of two target values, the pressure drop per unit length  $\Delta p / \Delta z$  and the local heat transfer coefficient  $h_{tp,j}$  are discussed.

The expanded uncertainty of the pressure drop per unit length  $u_e(\Delta p / \Delta z)$  has a value of 300 Pa/m. The main cause of the uncertainty is the calibration standard as well as the calibration process of the differential pressure transducer. The uncertainty of the distance between the pressure inlet and outlet taps (see Section 3.1) is negligible. The relative expanded uncertainty of all data points of this work has an average value of 5 %.

The expanded uncertainty of the local heat transfer coefficients  $u_e(h_{tp,j})$  depends on both the geometry parameters and thermal properties of the test section and the calibration of the sensors. Hence, the uncertainty varies with the local heat flux  $\dot{q}_j$ . The relative expanded uncertainty ranges from 20 % to 30 % for local heat fluxes greater than 15 kW/m<sup>2</sup>. At lower heat fluxes, the relative expanded uncertainty can exceed 30 %, whereby the parasitic heat input from the environment (see Eq. (19)) particularly affects the measurement data.

As already explained by Weise et al. [6] the presented uncertainty analysis is based on very conservative estimates of the individual uncertainty contributions. Against this background, the repeatability of the pressure drop and local heat transfer measurements is investigated to further assess the quality of the data points. In Fig. 4 the results of

exemplary repeatability experiments of the Kelvin cells are shown. Thereby, the same operating conditions were investigated on different days.

The pressure drop per unit length is depicted as a function of the mass flux (left) and the local heat transfer coefficients as a function of the local heat fluxes (right). The repeatability of the data points is evaluated in form of the mean absolute percentage repeatability (MAPR), which is calculated according to Eq. (21). The variable  $a$  corresponds to the respective target value and the indices 1 and 2 refer to the first and the repeated measurement. The parameter  $N$  equals the total number of data points.

$$MAPR = \frac{100}{N} \sum_{j=1}^N \left| \frac{a_1 - a_2}{a_1} \right| \quad (21)$$

In case of the pressure drop per unit length, an excellent repeatability is obtained for various mass fluxes ( $\dot{m}_0 \approx 25 \text{ kg}/(\text{m}^2\text{s}) - 100 \text{ kg}/(\text{m}^2\text{s})$ ) and vapor qualities ( $\dot{x}_{is} \approx 0.14 - 0.94$ ) with a MAPR of 4 %. Thereby, the repeatability of all data points is within the expanded uncertainty with an average value of 8 %.

Regarding the repeatability of the local heat transfer coefficients, two operating conditions with varying heat flux were evaluated, one of which ( $\dot{m}_0 \approx 75 \text{ kg}/(\text{m}^2\text{s}); \dot{x}_{PMI} \approx 0.5$ ) is depicted in Fig. 4. Thereby, in accordance to the pressure drop measurements an excellent repeatability with a MAPR of 4 % is achieved. The repeatability of all data points is significantly lower than the expanded uncertainty with an average value of 37 %.

In addition, repeatability measurements of the pressure drop per unit length ( $\dot{m}_0 \approx 140 \text{ kg}/(\text{m}^2\text{s}) - 185 \text{ kg}/(\text{m}^2\text{s}); \dot{x}_{is} \approx 0.5$ ) and the local heat transfer coefficients ( $\dot{m}_0 \approx 125 \text{ kg}/(\text{m}^2\text{s}); \dot{x}_{PMI} \approx 0.1$ ) were performed for the cubic cells, yielding comparable results. Consequently, a high quality of the measurement data of the target values is ensured for both POCS investigated.

**Table 2**

Overview of the varied process parameters and their value range. The maximum permissible time-dependent standard deviation of each parameter during the data acquisition is shown in brackets.

| Process parameter                                         | cubic cells        | Kelvin cells       |
|-----------------------------------------------------------|--------------------|--------------------|
| System pressure $p$ / bar                                 | 12 – 26.5 (0.01)   | 12 – 26.5 (0.01)   |
| Mass flux $\dot{m}_0$ / $\text{kg m}^{-2} \text{ s}^{-1}$ | 25 – 190 (1.5)     | 25 – 175 (1.5)     |
| Vapor quality $\dot{x}_{is}$ / –                          | 0.11 – 0.98 (0.01) | 0.11 – 0.97 (0.01) |
| Local heat flux $\dot{q}_j$ / $\text{kW m}^{-2}$          | 0.3 – 57 (0.3)     | 0.3 – 57 (0.3)     |

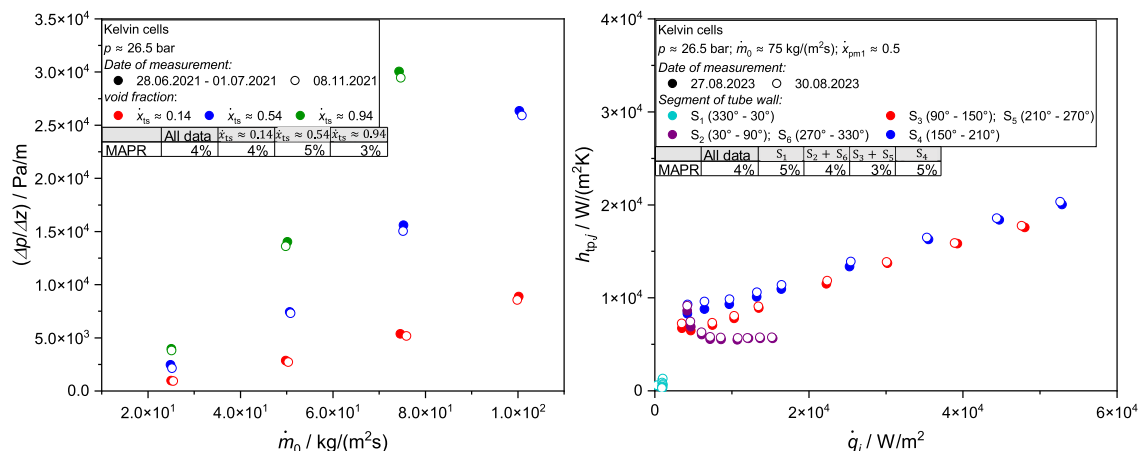


**Fig. 4.** Repeatability of the pressure drop measurements (left) and heat transfer measurements (right) of the kel at different operating conditions.

### 3.4. Investigated process parameters

In Table 2 an overview of the value range of all investigated process parameters is given. To ensure quasi-steady-state process conditions during the data acquisition, a threshold for the time-dependent standard deviation of each parameter was defined. Its value is shown in brackets behind the corresponding parameter. For the cubic cells, diabatic measurements were conducted exclusively at a system pressure of 26.5 bar.

## 4. Results and discussion

In this chapter, the deviations between the measurement data and the various model approaches are expressed in the form of the mean absolute percentage error (MAPE), which is calculated according to Eq. (22). In this regard  $a_{\text{exp}}$  and  $a_{\text{mod}}$  correspond to the experimentally determined and modelled target values.

$$\text{MAPE} = \frac{100}{N} \sum_{j=1}^N \left| \frac{(a_{\text{exp}} - a_{\text{mod}})}{a_{\text{exp}}} \right| \quad (22)$$

### 4.1. Pressure drop

First, the applicability of the pressure drop model developed for solid sponges from Weise et al. [22] (see Section 2.2) to the experimental data of this work is investigated. The acceleration pressure drop component due to evaporation (see Appendix B) of all data points is estimated to be at least two orders of magnitude smaller than the total pressure drop.

In Fig. 5 all data points of the experimental pressure drop per unit length  $(\Delta p / \Delta z)_{\text{exp}}$  under adiabatic (blue) and diabatic (red) conditions with the cubic cells (left) and the Kelvin cells (right) are compared with Eq. (7). In this respect, diabatic and adiabatic conditions refer to measurements with  $(\dot{q}_{\text{ts}} = 3 - 30.5 \text{ kW/m}^2)$  and without heat input in the test section.

For both structures, no systematic difference between adiabatic and diabatic pressure drop per unit length is observed, confirming the results of the above estimation of the acceleration pressure drop component due to evaporation. By additionally treating the vapor phase as incompressible (see Appendix B), the influence of the acceleration pressure drop is neglected in the remainder of this work.

For the Kelvin cells, the pressure drop model achieves a reasonable agreement with a MAPE of 34 %. The model correctly reproduces the functional relationship between the operating parameters and the pressure drop per unit length, yet a systematic offset is observed. For the structures with cubic cell geometry, very high deviations with a MAPE of 194 % are found. The model severely overestimates the pressure drop

per unit length of all data points.

Two assumptions of the model are conceivable as possible causes for the moderate deviations of the Kelvin cells and high deviations of the cubic cells.

Firstly, a linear relationship between the tortuosity and the total specific surface area is assumed by Inayat et al. [33] for solid sponges, which may not be generally transferable to POCS due to their large morphological differences. In this context, Kelvin cells represent an idealized substitute structure of solid sponges, wherefore the assumptions of Inayat et al. [33] apply with the exception of the regular cell geometry. For cubic cells, on the other hand, there are major structural differences to solid sponges (see Fig. 3), which could impair the applicability of the model. The above explanations are supported by the results of Woodward et al. [41], who investigated the single-phase pressure drop in cubic and Kelvin cells. Thereby, their measurement data of Kelvin cells is well described using the tortuosity according to Inayat et al. [33], whereas the data of cubic cells suggests significantly lower values of the tortuosity.

Additionally, the authors want to emphasize the difference between the geometric tortuosity and the hydrodynamic tortuosity. While the former is calculated based on the geometry of the porous structure, the latter is also influenced by the velocity as shown by Meinicke [42] and Duda et al. [43]. As a result, the calculation of tortuosity according to Eq. (9) could cause an overestimation of the Forchheimer coefficient and thus of the pressure drop.

The second cause, which in particular could explain the high deviations of the cubic cells, lies within the use of the homogeneous model. Thereby, it is assumed that porous structures enhance the momentum exchange between the phases and thus reduce the slip ratio. However, in contrast to solid sponges, both investigated POCS and especially the cubic cells, exhibit straight fluid paths (see Fig. 3), which could lead to a reduced momentum exchange and therefore an increase of the slip ratio.

Based on the above findings, the alternative model approach presented in Eq. (11), which does not rely on the tortuosity, is examined for two different two-phase flow methods (homogenous model, drift flux model according to Rouhani [29]). The comparison of the alternative model with the experimental pressure drop per unit length (adiabatic, diabatic) is depicted in Fig. 6.

In accordance with the previous results, no difference between adiabatic and diabatic data is found. For the Kelvin cells, the best modelling result was obtained using the homogenous model (Fig. 6, top right) with a MAPE of only 11 %. Considering slip with the drift flux model (Fig. 6, bottom right), the MAPE increases to 24 %. It is assumed that the Kelvin cells, due to their structural similarity to solid sponges, provide a similar momentum exchange between the phases and thus a

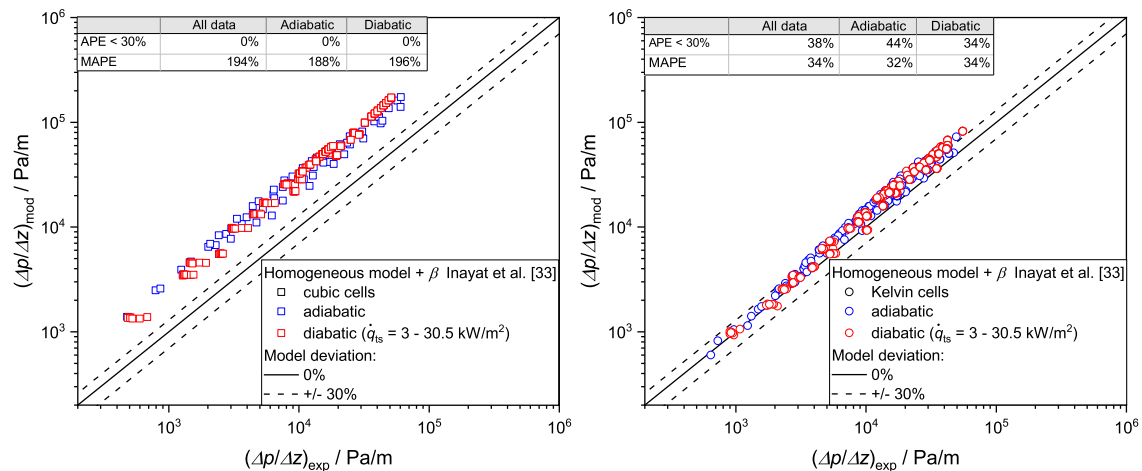


Fig. 5. Comparison of the adiabatic (blue) and diabatic (red) pressure drop per unit length of cu (left) and kel (right) with the model of Weise et al. [22]. The Forchheimer coefficient is calculated according to Inayat et al. [33].

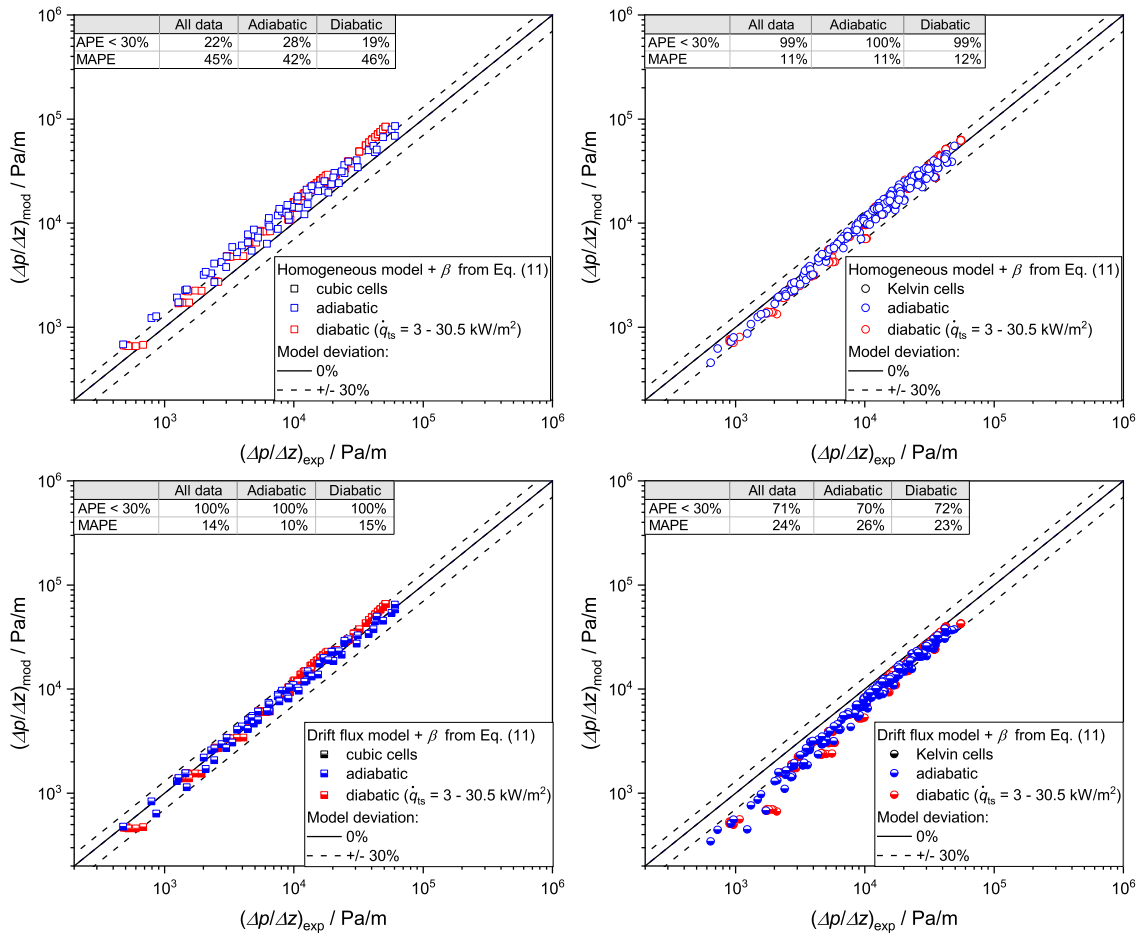


Fig. 6. Comparison of the adiabatic (blue) and diabatic (red) pressure drop per unit length of cu (left) and kel (right) with the alternative model approach from Eq. (11). The model is presented with no slip between the phases (homogenous model, top) and slip between the phases (drift flux model, bottom).

reduction of the slip. This assumption is supported by the relatively good agreement of the measurement data with Eq. (7). For the structures with cubic cell geometry, the drift flux model (Fig. 6, bottom left) with a MAPE of 14 % yields a substantially better result than the homogeneous model (Fig. 6, top left) with a MAPE of 45 %. It is assumed that the cubic cell geometry in terms of its projected free cross-sectional area (see Fig. 1) leads to less mixing of the phases and thus favors slip. In general, the alternative model approach provides significantly better results for the cubic cell geometry, regardless of the two-phase flow method used.

For a closer look at the influence of different process parameters on the functionality of the model, Fig. 7 shows the data points subdivided into the investigated system pressures  $p$  and average vapor qualities in the test section  $x_{ts}$ . The homogeneous model is used for the Kelvin cells and the drift flux model for the cubic cells. An examination of the MAPE of the various operating conditions shows that for both cell types, the influence of the system pressure and vapor quality on the flow velocity ( $u_m = m_0/\rho_m$ ) and thus the pressure drop is adequately represented by the respective two-phase flow method. The model has an almost constant predictive power over the entire range of operating parameters. This also applies to the investigated data range of the mass flux  $\dot{m}_0$  (see Table 2).

To summarize the above findings, the pressure drop of two-phase flows through Kelvin cells can be modelled in accordance to solid sponges by combining the homogeneous model with the Forchheimer term, supporting the first hypothesis of this work (see Section 2.2). In case of the cubic cells, the hypothesis was disproven, as slip between the phases should be considered. This shows that the relation between the mixing of the phases and various cell geometries needs to be

investigated in more detail to quantify the influence of the cell type on the slip between the phases.

#### 4.2. Heat transfer

One of the main objectives of this chapter is to investigate whether the convective boiling heat transfer of two-phase flows within POCS (cu, kel) is described by the model presented in Section 2.3. Therefore, the approach of Kattan et al. [2] is chosen to extract the convective boiling heat transfer coefficient  $h_{cb,j}$  from the measurement data ( $h_{tp,j}$ ) for which Eq. (12) is rearranged for one segment  $j$  (see Eq. (23)).

$$h_{cb,j} = \sqrt[3]{h_{tp,j}^3 - h_{nb}^3(\dot{q}_{i,j})} \quad (23)$$

For the applicability of the above equation, two conditions must be met, which are investigated in Sections 4.2.1 and 4.2.2. The respective segment  $j$  must be completely wetted ( $f_{dry,j} = 0$ ) and the nucleate boiling heat transfer contribution (see Section 4.2.2) must be known. Subsequently, the convective boiling heat transfer is investigated in Section 4.2.3.

As the second main objective of this chapter, the superposition of the heat transfer of the liquid and vapor phase is investigated. Therefore, the circumferentially averaged heat transfer of partially and completely wetted segments is evaluated in Section 4.2.4.

##### 4.2.1. Wetting of the tube wall

As explained in Section 2.3, porous inserts influence the flow patterns and thus the wetting of the tube wall. The aim of this section is to

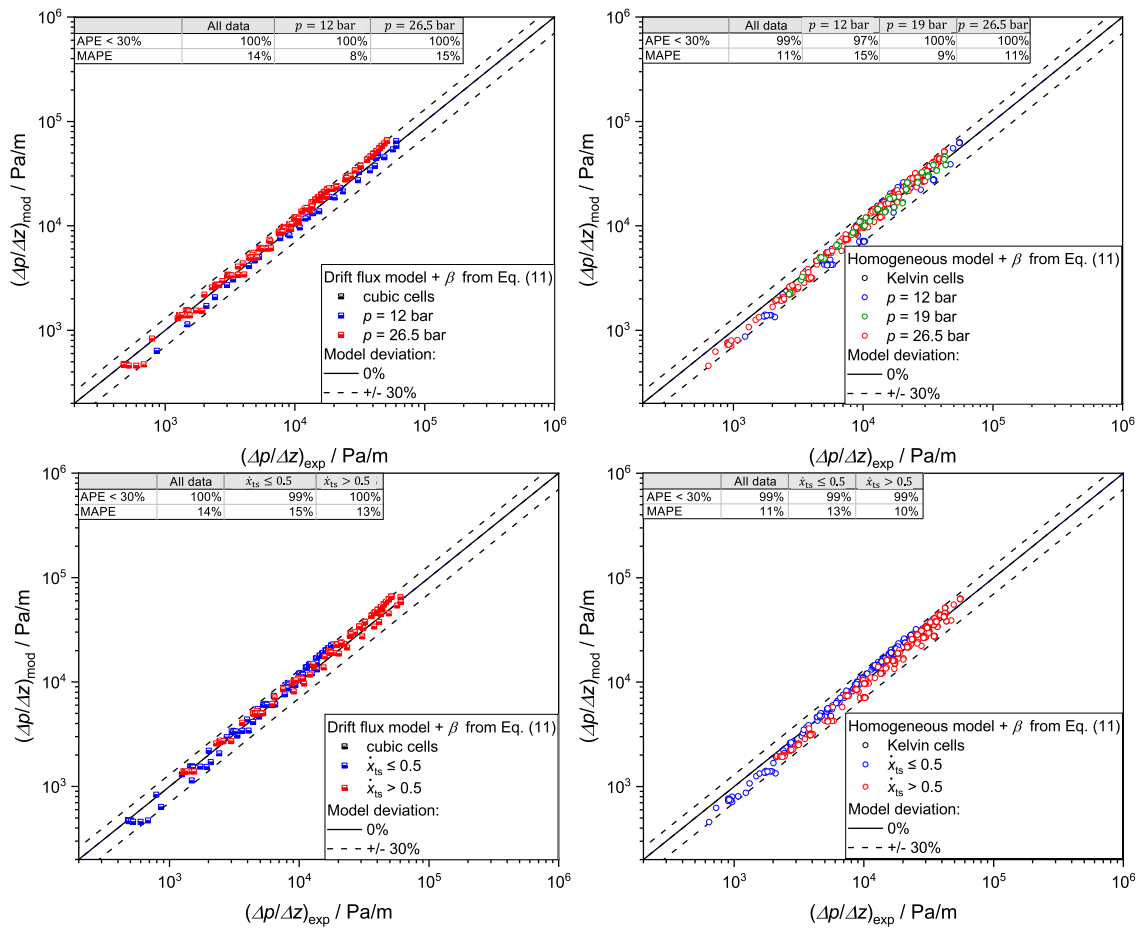


Fig. 7. Comparison of the pressure drop per unit length of cu (left) and kel (right) to the alternative model approach from Eq. (11). The data is subdivided into system pressure  $p$  (top) and vapor quality  $\dot{x}_{ts}$  (bottom).

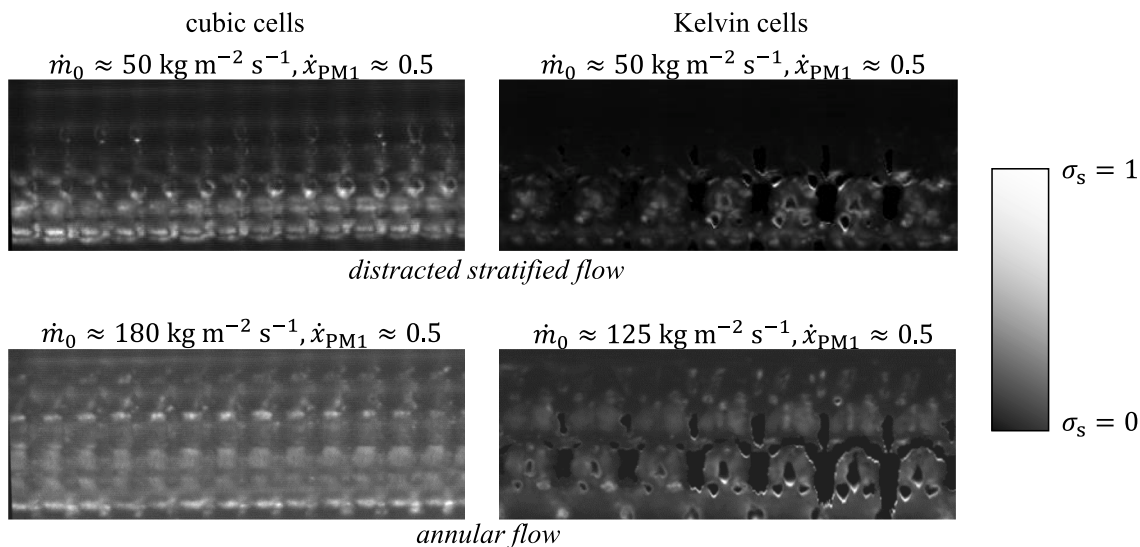


Fig. 8. Standard deviation  $\sigma_s$  of each pixel of the high-speed video recordings normalized to gray scale values for cu and kel (left and right) with partial wetting of the tube wall (distracted stratified flow, top) and complete wetting of the tube wall (annular flow, bottom).

derive a simple criterion to approximate the wetting of the tube wall. Hence, only two flow patterns (distracted stratified and annular flow) with partial and complete wetting of the tube wall are distinguished. It is important to emphasize that it is by no means the goal of this section to develop flow pattern maps that can be universally applied to POCS.

Both high-speed video recordings (500 fps) and an evaluation of the heat transfer in the top segment ( $S_1$ ) are used to determine the respective flow pattern.

Fig. 8 shows the results of the high-speed video recordings of one exemplary distracted stratified and annular flow for each POCS (cu, kel).

The video recordings are presented in form of the standard deviation of each pixel, normalized to gray scale values ( $\sigma_s$ ). A high standard deviation (white color) represents a strong fluctuation of the phase boundary. Thereby, the annular flow differs from the distracted stratified flow in that the phase boundary is present over the entire cross-section of the tube, thus the entire tube wall is assumed to be wetted. When comparing the structures, it is noticeable that much higher mass fluxes are required for the cubic cells to achieve an annular flow. In agreement with the results of the pressure drop modeling (see Section 4.1), the cell geometry is identified as the cause for the worsened wetting. Thereby, the straight fluid paths of the cubic cells favor an accumulation of the liquid phase at the tube bottom. For a detailed description of the image processing routine, the reader is referred to [6].

The above video recordings were carried out in adiabatic and diabatic operation of the test section, whereby no influence of the heat input on the results was observed. An evaluation of the respective heat transfer data suggests that the top segment ( $S_1$ ) could be completely wetted, even if the video recordings suggest distracted stratified flow. Consequently, a second method to determine the wetting of the tube wall is used. In this regard, Weise et al. [6] found that the heat transfer in the upper segments ( $S_1, S_2, S_6$ ) is almost identical, when the tube wall is completely wetted and differs only within the repeatability range of the measurement data (see Section 3.3). Accordingly, the ratio of the heat transfer coefficient of the top segment ( $h_{tp,S_1}$ ) and the arithmetic mean of segment 2 and 6 ( $\bar{h}_{tp,S_2,S_6}$ ) is determined. Values greater or equal to 0.9 are interpreted as complete wetting of  $S_1$  and therefore the entire tube wall (annular flow).

Fig. 9 shows the results of both methods as a function of the mass flux  $\dot{m}_0$  and the vapor quality at the plane of measurement 1 ( $\dot{x}_{pm1}$ ) for a system pressure  $p$  of 26.5 bar.

The symbol color (blue, gray) stands for the results of the high-speed recordings and the filling of the symbols for those of the heat transfer measurements. For both POCS (cu, left and kel, right), the required mass flux for complete wetting ( $\theta_{dry} = 0$ ) sinks with increasing vapor quality. As mentioned above a clear discrepancy between the video recordings and heat transfer measurements is found, whereby the top segment ( $S_1$ ) appears to be wetted at lower mass fluxes than the video recordings suggest. As a result, an individual mass flux  $\dot{m}_{0,a}$  (black dashed line) was determined for each POCS at which complete wetting can be guaranteed at all operating conditions according to both methods. The same procedure was applied to a system pressure of 12 bar for the Kelvin cells,

where a decrease in the value of  $\dot{m}_{0,a}$  was found. Here, the reduced vapor density leads to higher vapor velocities at the same mass fluxes and thus to a better transport of the liquid phase to the top of the tube. Subsequently, with the use of Eq. (C.2) in Appendix C a simple criterion for checking all segments for complete wetting is obtained. The criterion deliberately underestimates the wetting at high vapor qualities.

#### 4.2.2. Nucleate boiling

For the use of Eq. (23), it is examined whether the model of Cooper [35] describes the nucleate boiling heat transfer with POCS, as it does for empty tubes and solid sponge inserts [1–3,6,8]. In this regard, only the bottom segment ( $S_4$ ) is considered in the following evaluation, as it is completely wetted at all operating conditions according to Eq. (C.2). Fig. 10 shows the experimental heat transfer coefficients of segment 4 (cu, left; kel, right) as a function of the heat flux  $\dot{q}_{S_4}$ .

The model of Cooper [35] corresponds to the black line. Only data points at a system pressure of 26.5 bar are depicted, as for these the nucleate boiling contribution is increased due to its material property dependence (surface tension, liquid and vapor density). Consequently, the superposition of the nucleate boiling by the convective boiling heat transfer (see Eq. (12)) is reduced. At higher heat fluxes, a very good agreement is observed between the data points and the model of Cooper for both cell types (cu,  $\dot{q}_{S_4} > 10 \text{ kW/m}^2$  and kel,  $\dot{q}_{S_4} > 20 \text{ kW/m}^2$ ) with a MAPE of 8 % and 19 %, respectively. For data points at lower heat fluxes (cu,  $\dot{q}_{S_4} \leq 10 \text{ kW/m}^2$  and kel,  $\dot{q}_{S_4} \leq 20 \text{ kW/m}^2$ ), the contribution of convective boiling heat transfer increases and the MAPE rises to 27 % and 51 %, respectively. Thereby, the convective boiling heat transfer completely dominates at high mass fluxes and vapor qualities (see horizontal progression of data points).

Based on the above findings, it is confirmed that the nucleate boiling heat transfer for both POCS investigated also follows the model of Cooper (see Eq. (17)), just like empty tubes. Regarding the underlying physical phenomenon, we assume the nucleation sites to be unaffected compared to the empty tube, whereby the high contact resistances between the POCS and the tube wall (clearance fit, see Section 3.1) inhibit the generation of additional nucleation sites. However, similar to fins the POCS influence the flow characteristics, like the flow pattern or the velocity gradient adjacent to the tube wall, affecting the convective boiling. Accordingly, in the next step, Eq. (17) is used in Eq. (23) to determine the convective boiling heat transfer coefficients of completely

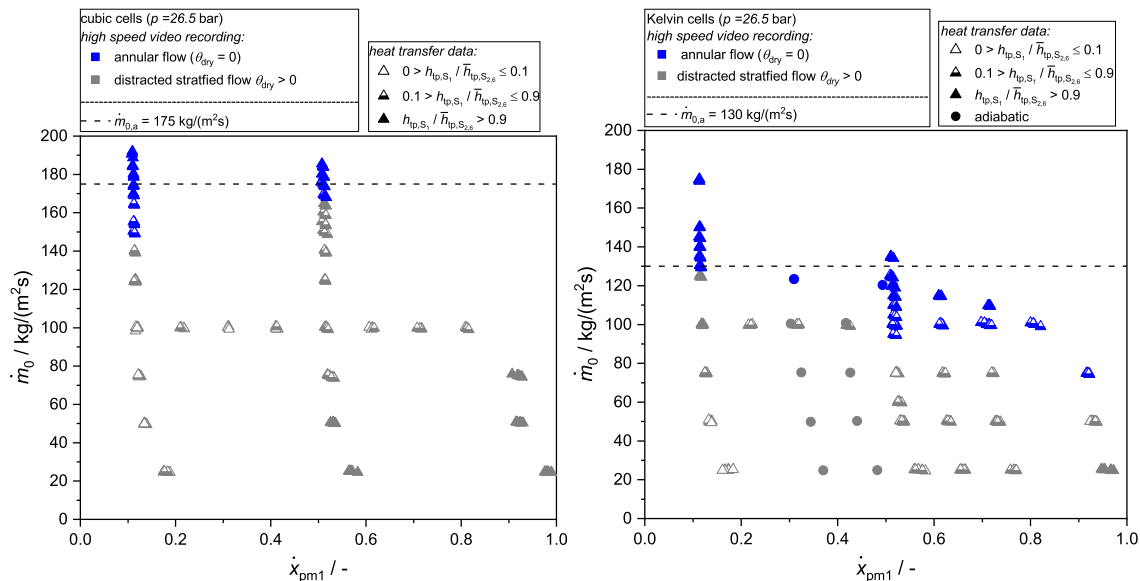


Fig. 9. Differentiation between complete wetting of the tube wall (annular flow) and partial wetting of the tube wall (distracted stratified flow) based on the high-speed video recordings and heat transfer measurements. The cu are shown on the left and the kel on the right.

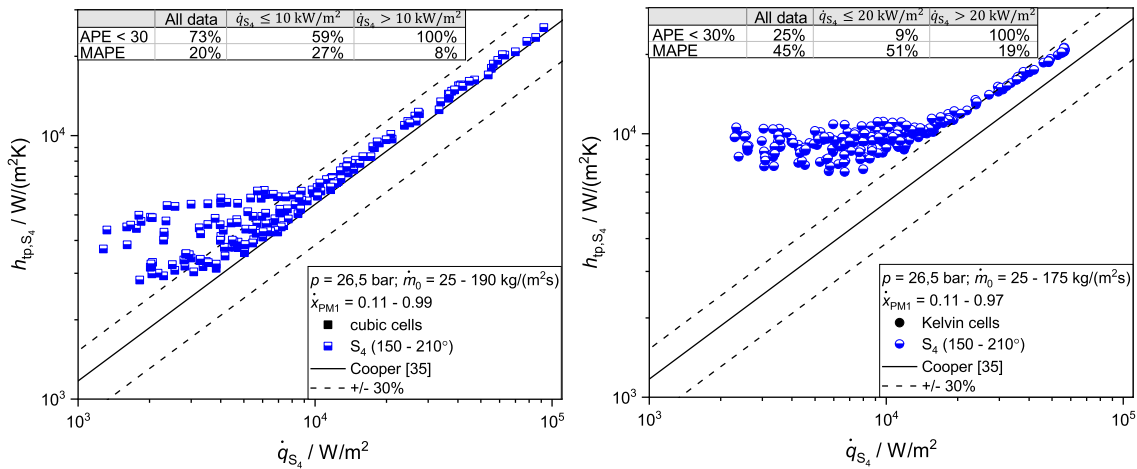


Fig. 10. Comparison of the heat transfer coefficient at the bottom segment ( $S_4$ ) with the model of Cooper [35] (black line) at a system pressure  $p$  of 26.5 bar. The cu are shown on the left and the kel on the right.

wetted segments.

4.2.3. Convective boiling

For the use of Eq. (23), the two criteria mentioned below were defined, based on which data points of the two-phase heat transfer of each segment ( $S_1 - S_6$ ) were selected.

- Complete wetting of the evaluated segments  $j$  according to Eq. (C.2)
- Two-phase heat transfer is not dominated by nucleate boiling  $h_{cb,j} / h_{nb}(\dot{q}_{i,j}) \geq 1$

The reason for the data selection is that in the case of partial wetting of a segment  $j$ , both heat transfer of the liquid and vapor phase occur. Due to the uncertainty in the determination of the dry angle as well as the superposition of the heat transfer of the liquid and vapor phase, such data points are unsuitable for evaluation.

In addition, the selected data points are restricted to operating conditions with high contribution of the convective boiling heat transfer

$h_{cb,j} / h_{nb}(\dot{q}_{i,j}) \geq 1$ , as otherwise nucleate boiling dominates and the convective boiling heat transfer cannot accurately be extracted from the cubic averaging (see Eq. (23)).

Under consideration of the above criteria, a total of 336 data points of the cubic cells and 842 data points of the Kelvin cells were selected.

To evaluate the influence of the POCS on the convective boiling, the measurement data is first compared with an established convective boiling model for empty tubes. The model of Kattan et al. [2] is chosen, as it is in good agreement with the CO<sub>2</sub> data for empty tubes [1]. All relevant equations of the model are included in Appendix C.

In Fig. 11 the data points of the convective boiling at a system pressure 26.5 bar of the cubic cells (left) and the Kelvin cells (right) are compared to the empty tube model. The Nusselt number  $Nu_{cb}$  is depicted as a function of the Reynolds number of the liquid phase  $Re_L$ . For a clearer understanding, only the mean values of the lower ( $S_3, S_4, S_5$ ) and upper half ( $S_1, S_2, S_6$ ) of the tube are shown.

All data points of the POCS (cu, kel) are systematically underestimated, with MAPE exceeding 60%. It is assumed that the POCS

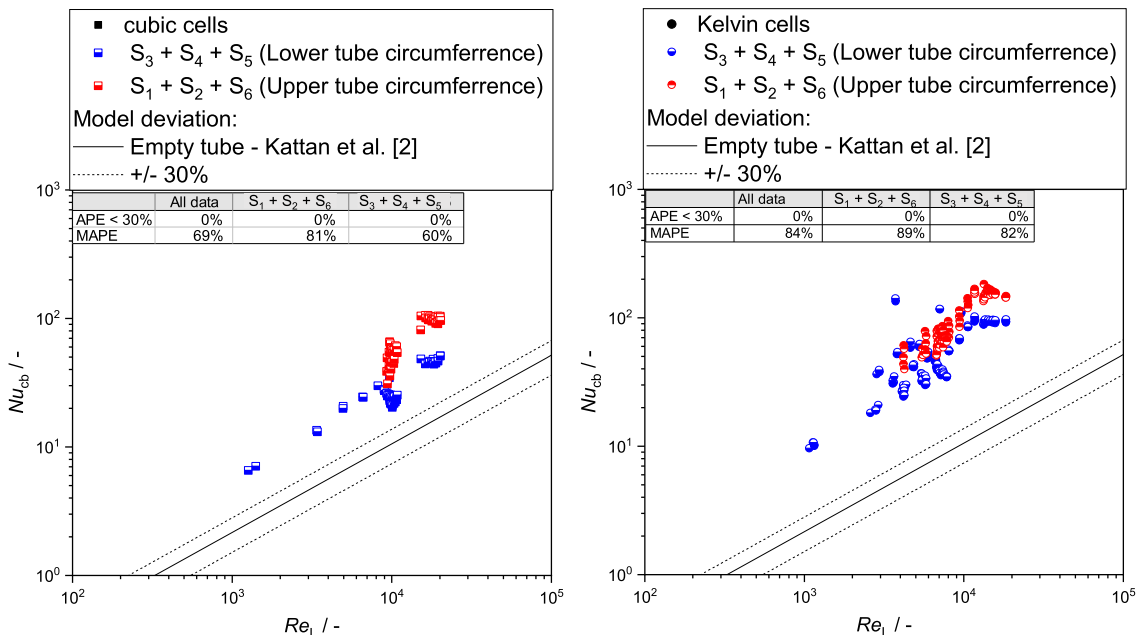


Fig. 11. Comparison of the convective boiling heat transfer of completely wetted segments with the empty tube model of Kattan et al. [2] for cu (left) and kel (right).

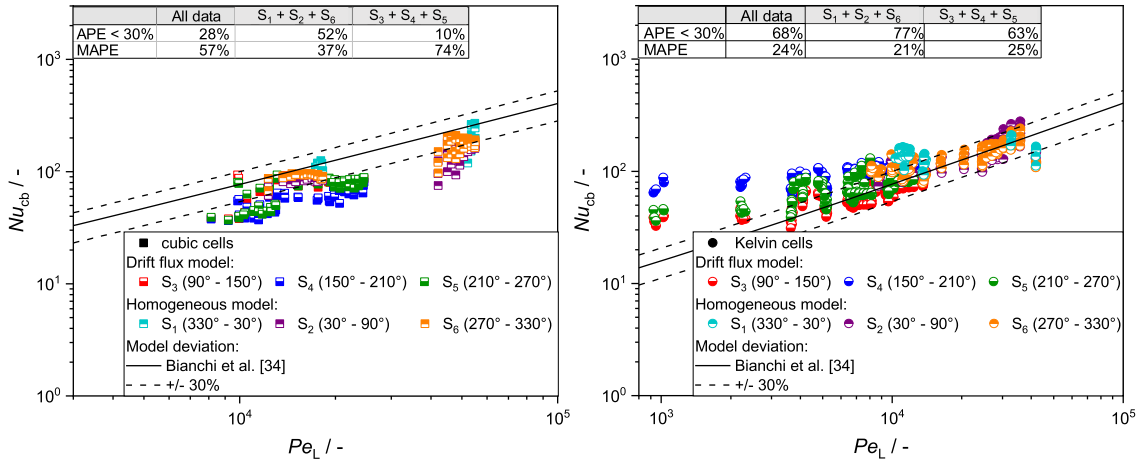


Fig. 12. Comparison of the convective boiling heat transfer of completely wetted segments with the model of Bianchi et al. [34] modified according to Weise et al. [6] for cu (left) and kel (right).

increase the velocity gradients adjacent to the tube wall by redirecting the two-phase flow, which leads to increased convective boiling heat transfer. Additionally, the heat transfer in the upper half of the tube (S<sub>1</sub>, S<sub>2</sub>, S<sub>6</sub>) is higher than in the lower half (S<sub>3</sub>, S<sub>4</sub>, S<sub>5</sub>), the causes are examined in more detail below. The scattering of the data points (e.g., S<sub>3</sub>, S<sub>4</sub>, S<sub>5</sub> with kel) results from the characteristic length scale of the empty tube model (film thickness, see Appendix C), which does not scale correctly with the convective boiling heat transfer with porous inserts. The data indicates, that POCS as inserts lead to a significant intensification of the convective boiling heat transfer. At this point it should be noted, that an evaluation of the performance of the structures using e.g., thermal enhancement factors is not part of this work and is examined separately.

Based on the above findings, the measurement data is now compared to a convective boiling model for solid sponge inserts (see Section 2.3). In Fig. 12 the data points of the convective boiling heat transfer in form of the Nusselt number  $Nu_{cb}$  are compared to the model of Bianchi et al. [34] (see Eq. (14)). The data points cover a range of the Péclet number  $Pe_L$  of  $8 \cdot 10^3 - 5.5 \cdot 10^4$  and  $9 \cdot 10^2 - 4.2 \cdot 10^4$  for the cubic and Kelvin cells, respectively.

Thereby, the data points of the Kelvin cells (right) exhibit a predominantly good agreement with the model, with a MAPE of 24%. However, it is noticeable that the functional relationship between the Nusselt and Péclet numbers is not correctly represented as the deviations increase up to 82% with decreasing Péclet numbers. Nevertheless, the

generally good agreement of the data points with the model is attributed to the high structural similarity of Kelvin cells to solid sponges. In the case of the cubic cells (left), the deviations between the model and the data points are significantly increased, resulting in a MAPE of 57%. Here, the model overestimates the data points over the entire range of operating parameters. In accordance with the pressure drop modeling (see Section 4.1), it is assumed that the cubic cell geometry with its straight fluid paths leads to a reduced redirection/mixing of the phases and therefore reduced convective boiling heat transfer.

In agreement with the results of Weise et al. [6], the heat transfer in the upper half of the tube (S<sub>1</sub>, S<sub>2</sub>, S<sub>6</sub>) is increased by up to one order of magnitude compared to the lower half of the tube (S<sub>3</sub>, S<sub>4</sub>, S<sub>5</sub>) for both cell types. Consequently, in accordance to solid sponges the use of the homogeneous model for the upper half of the tube (S<sub>1</sub>, S<sub>2</sub>, S<sub>6</sub>) and the use of the drift flux model for the lower half of the tube (S<sub>3</sub>, S<sub>4</sub>, S<sub>5</sub>), yields a good agreement between modeling results and experimental data. A potential explanation for this effect presents the stratification of the phases caused by gravity. Due to the locally larger void fraction in the upper half of the tube, the momentum exchange of the phases is improved, hence slip is reduced and consequently higher flow velocities of the liquid phase are achieved.

The observations do not contradict the results of the pressure drop modeling (see Section 4.1), since for modelling the local convective boiling heat transfer coefficients also the local flow velocities have to be considered.

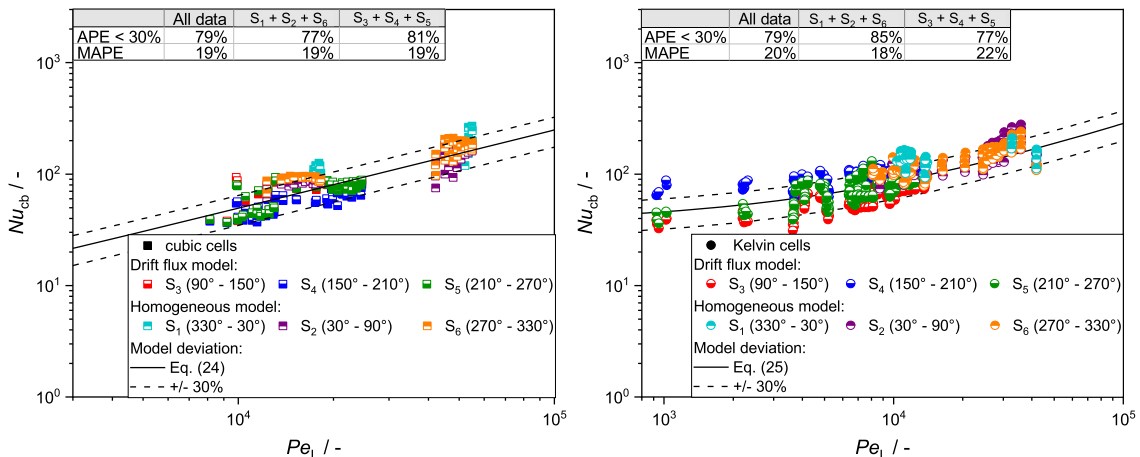


Fig. 13. Comparison of the convective boiling heat transfer of completely wetted segments with Eq. (24) for cu and Eq. (25) for kel.

To achieve better modeling results, slight adjustments were made to the heat transfer model of Bianchi et al. [34] with Eqs. (24) and (25). Despite the different geometries of cubic and Kelvin cells, both models follow the same functional relationship between the Nusselt and the Péclet number and differ only in one empirical parameter. However, it should be emphasized that the models are limited to the investigated Péclet range. An extension of the range of validity, especially to lower Péclet numbers, requires further measurements.

$$\text{cu} : Nu_{cb} = 1 + 0.07 \cdot (Pe_L)^{0.71} \quad (24)$$

$$\text{kel} : Nu_{cb} = 36.48 + 0.07 \cdot (Pe_L)^{0.71} \quad (25)$$

Fig. 13 shows the comparison of the above equations with the data points of the convective boiling heat transfer. Thereby, a MAPE of 20 % and 19 % is obtained for the cubic and Kelvin cells, respectively.

For the cubic cells, a significantly improved modeling result is achieved over the entire range of operating parameters, where the data points are no longer systematically overestimated by the model. Regarding the Kelvin cells, especially the data points at low Péclet numbers, are modelled with higher accuracy.

To conclude the above findings for completely wetted segments, the first hypothesis from Section 2.3, according to which the convective boiling heat transfer of both cell types is described by the model of Bianchi et al. [34] was falsified. The second hypothesis was verified, as much better modelling results were obtained for both cell types with the homogeneous model being used in the upper half and the drift flux model being used in the lower half of the tube.

#### 4.2.4. Circumferentially averaged heat transfer

In the last step of the heat transfer evaluation, the third hypothesis from Section 2.3 is investigated, according to which the circumferentially averaged heat transfer using POCS also follows a superposition of the liquid and vapor phase. Against this background, a comparison of all data points of this work ( $h_{tp,exp}$ ) of both POCS (cu, blue and kel, red) with Eq. (12) is depicted in Fig. 14. The data points contain both partial and complete wetting of the tube wall.

Here, the convective boiling heat transfer and convective heat transfer of the vapor phase are determined with Eqs. (24) and (25). Thereby, the Péclet number is calculated depending on the phase (vapor, liquid) as explained in Section 2.3. The dry angle of the tube ( $\theta_{dry}$ ) is determined with Eq. (C.2) and distributed symmetrically over the circumference, starting at the top segment ( $S_1$ ). A visualization of the procedure is given in the Appendix C.

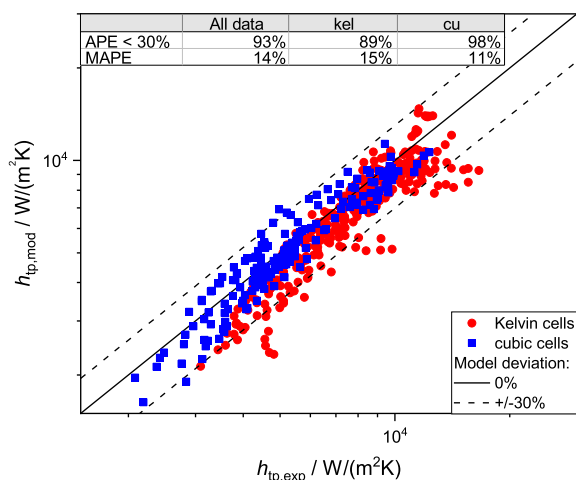


Fig. 14. Comparison of the circumferentially averaged heat transfer coefficient at complete and partial wetting of the tube wall with Eq. (12). The contribution of the convective boiling and the convective heat transfer of the vapor phase are calculated according to Eqs. (24) and (25), respectively.

With a MAPE of 11 % for the cubic cells and 15 % for the Kelvin cells, a good modeling result is obtained for both POCS. For the Kelvin cells, some data points are underestimated with deviations exceeding 30 %. All corresponding data points have high vapor qualities ( $x_{pm1} > 0.6$ ), for which the wetting of the tube wall and thus the average heat transfer coefficient is underestimated due to the conservatively chosen wetting criteria (see Section 4.2.1). Nevertheless, despite the simplistic determination of the wetting of the tube wall the above model provides very good results.

In summary, the hypothesis according to which the average heat transfer follows a superposition of the heat transfer of the vapor and the liquid phase is confirmed for both POCS investigated. Furthermore, the good results at lower vapor qualities ( $x_{pm1} \leq 0.6$ ) for the Kelvin cells and all vapor qualities for the cubic cells with partial wetting of the tube wall indicate that the convective heat transfer of the vapor phase is also well represented by Eqs. (24) and (25).

## 5. Conclusion

In this work, the pressure drop and heat transfer during flow boiling of CO<sub>2</sub> in a horizontal tube with periodic open cellular inserts were investigated. Two structures with cubic and Kelvin cells with nominal open porosities of 83 % were examined.

Both the adiabatic and diabatic pressure drop data was modelled successfully by combining an established single-phase pressure drop model for POCS of Klumpp et al. [15] with a suitable two-phase flow method. The pressure drop data of the Kelvin cells follows the homogeneous model without slip between phases ( $u_v = u_L$ ), whereas the pressure drop data of the cubic cells is well described by the drift flux model with slip between phases ( $u_v \neq u_L$ ). It is assumed that the straight fluid paths of the cubic cells cause less momentum exchange between phases, thus favoring slip. The new pressure drop model describes the data with a MAPE of 14 % and 11 % for the cubic and Kelvin cells, respectively.

The heat transfer measurements were carried out discretely by subdividing the circumference of the test section into 6 segments ( $S_1$ - $S_6$ ) of 60° each. In the course of the heat transfer modeling, the individual influencing factors were evaluated step by step. First, it was shown that the nucleate boiling heat transfer follows the model of Cooper [35], which is established for empty tubes and solid sponges. In the next step, based on high-speed video recordings of the flow patterns and an evaluation of the heat transfer in the upper half of the tube ( $S_1, S_2, S_6$ ), a simple criterion for complete wetting of the tube wall was defined. Subsequently, the convective boiling heat transfer of completely wetted segments was determined following the procedure of Kattan et al. [2]. In agreement with the findings of Weise et al. [6] for solid sponges, it was found that the convective boiling heat transfer in the upper half of the tube ( $S_1, S_2, S_6$ ) follows the homogeneous model while the lower half of the tube ( $S_3, S_4, S_5$ ) can be described by the drift flux model with regard to the void fraction. Thereafter, a separate model of the convective boiling heat transfer for each POCS (cu, kel) was derived from the measurement data.

The models cover a range of the Péclet number of  $8 \cdot 10^3 - 5.5 \cdot 10^4$  and  $9 \cdot 10^2 - 4.2 \cdot 10^4$  and describe the data points with a MAPE of 19 % and 20 % for the cubic and Kelvin cells, respectively. Thereby, it was found that the convective boiling heat transfer of the Kelvin cells is up to one order of magnitude greater than the one of the cubic cells at the same operating conditions. Again, the cell geometry is assumed to be the cause, according to which the straight fluid paths of the cubic cells result in a reduced redirection/mixing of the phases and hence a reduced convective boiling heat transfer.

In the last step of the evaluation, the circumferentially averaged heat transfer was found to follow a superposition of the heat transfer of the liquid and vapor phase in accordance to empty tubes and solid sponges [2,6]. By calculating the nucleate boiling contribution according to

Cooper [35], the convective boiling heat transfer and convective heat transfer of the vapor phase with the corresponding model of each POCS, a MAPE of 11 % and 15 % was obtained for the cubic and Kelvin cells, respectively.

With regard to future work, it is recommended to investigate the local distribution of the void fraction over the cross-section of horizontal tubes with POCS in order to better understand the influence of the cell geometry on the mixing of the phases (flow patterns) and consequently the slip.

### CRedit authorship contribution statement

**Jonas Bender:** Conceptualization, Data curation, Formal analysis, Investigation, Methodology, Validation, Visualization, Writing – original draft. **Konrad Dubil:** Conceptualization, Formal analysis, Methodology, Writing – review & editing. **Franz Korn:** Formal analysis, Investigation, Methodology. **Thomas Wetzels:** Conceptualization, Funding acquisition, Project administration, Resources, Supervision, Writing – review & editing. **Benjamin Dietrich:** Conceptualization,

Funding acquisition, Project administration, Resources, Supervision, Writing – review & editing.

### Declaration of competing interest

The authors declare that they have no known competing financial interests or personal relationships that could have appeared to influence the work reported in this paper.

### Data availability

Data will be made available on request.

### Acknowledgements

The authors would like to thank the German Research Foundation (DFG) for funding the Project WE 4672/2–2, within which the results reported here were achieved.

## Appendix A

In this section, equations for calculating the geometry parameters of the investigated POCS are presented.

For the determination of the nominal and experimental geometry parameters ( $d_{w,exp}$ ,  $d_{w,CAD}$ ,  $\psi_{o,CAD}$ ,  $S_{v,CAD}$ ) of the Kelvin and cubic cell structures the equations from Horneber [40] are used.

#### Experimental and nominal average window diameter ( $d_{w,exp}$ , $d_{w,CAD}$ ):

Both the experimental and the nominal average mean window diameter ( $d_{w,exp}$ ,  $d_{w,CAD}$ ) are calculated with Eq. (A.1) for Kelvin and with Eq. (A.2) for cubic cells. In each case the respective measured or nominal values of the strut length  $l_s$  and the diameter  $d_s$  are used.

$$d_{w,kel} = \frac{2}{\sqrt{7 \cdot \pi}} \left( (6 \cdot \sqrt{3} + 3) \cdot l_s^2 - 18 \cdot l_s \cdot d_s + (2 \cdot \sqrt{3} + 3) \cdot d_s^2 \right)^{1/2} \quad (A.1)$$

$$d_{w,cu} = \frac{2 \cdot (l_s - d_s)}{\sqrt{\pi}} \quad (A.2)$$

#### Nominal open porosity $\psi_{o,CAD}$ :

The nominal open porosity of the Kelvin cells  $\psi_{o,CAD,kel}$  is calculated according to Eq. (A.3) with  $a_{kel} = l_{s,CAD}/d_{s,CAD}$  being the dimensionless strut length.

$$\psi_{o,CAD,kel} = 1 - \frac{3 \cdot \pi}{8 \cdot \sqrt{2} \cdot a_{kel}^3} \cdot \left( a_{kel} + \frac{2}{3} - \frac{2 \cdot \sqrt{2}}{3} \right) \quad (A.3)$$

The nominal open porosity of the cubic cells  $\psi_{o,CAD,cu}$  is calculated according to Eq. (A.4) with  $a_{cu} = l_{s,CAD}/d_{s,CAD}$ .

$$\psi_{o,CAD,cu} = 1 - \frac{3 \cdot \pi}{4 \cdot a_{cu}^3} \cdot \left( a_{cu} + \frac{2}{3} - \frac{8 \cdot \sqrt{2}}{9} \right) \quad (A.4)$$

#### Nominal specific surface area $S_{v,CAD}$ :

The nominal specific surface area  $S_{v,CAD,kel}$  is calculated according to Eq. (A.5).

$$S_{v,CAD,kel} = \frac{3 \cdot \pi}{2 \cdot \sqrt{2} \cdot a_{kel}^3 \cdot d_s} \cdot (a_{kel} + \sqrt{2} - 2) \quad (A.5)$$

The nominal specific surface area  $S_{v,CAD,cu}$  is calculated according to Eq. (A.6).

$$S_{v,CAD,cu} = \frac{3 \cdot \pi}{a_{cu}^3 \cdot d_s} \cdot \left( a_{cu} + \sqrt{2} - \frac{7}{3} \right) \quad (A.6)$$

#### Experimental open porosity $\psi_{o,exp}$ :

The experimental open porosity of both structures was determined according to Eq. (A.7). The mass of each structure  $m_{struct,j}$  was measured with an analytical balance and the dimensions of the structures ( $d_{struct}$ ,  $l_{struct}$ ) were determined by means of a vernier caliper, assuming an ideal cylindrical geometry. A value of 2675 kg m<sup>-3</sup> [44,45] was used as the solid density  $\rho_{solid}$ . The inaccessible pore volume  $V_{inj}$  was extracted from the CT scans.

$$\psi_{o,exp,j} = 1 - \frac{\left( \frac{m_{struct,j}}{\rho_{solid}} - V_{inj} \right)}{\left( \frac{\pi}{4} \cdot d_{struct,j}^2 \cdot l_{struct,j} \right)} \quad (A.7)$$

#### Projected free cross-sectional area $A_{f,j}$ :

The projected free cross-sectional area of cubic cells is calculated according to Eq. (A.8).

$$A_{f, \text{cu}} = (l_s - d_s)^2 \quad (\text{A.8})$$

The projected free cross-sectional area of Kelvin cells is calculated according to Eq. (A.9).

$$A_{f, \text{kel}} = 2 \cdot (l_s - d_s)^2 + 4 \cdot (l_s - d_s) \cdot \left( \frac{3 \cdot l_s - d_s}{2} \right) \quad (\text{A.9})$$

**Total cross-sectional area  $A_{c,j}$ :**

The total cross-sectional area of cubic cells is calculated according to Eq. (A.10).

$$A_{c, \text{cu}} = l_s^2 \quad (\text{A.10})$$

The total cross-sectional area of Kelvin cells is calculated according to Eq. (A.11).

$$A_{c, \text{kel}} = \left( \frac{4}{\sqrt{2}} l_s \right)^2 \quad (\text{A.11})$$

## Appendix B

In this section, various equations required for modelling the single and two-phase pressure drop in porous structures are presented.

**Acceleration component of the pressure drop  $\left( \frac{\Delta p}{\Delta z} \right)_{\text{acc}}$ :**

Depending on the two-phase flow method used (homogeneous model, drift flux model), the acceleration component (acc) due to evaporation can be estimated according to Müller and Steiner [46] using Eq. (B.1) or (B.2). Thereby, the vapor and liquid phases are assumed incompressible and therefore expansion evaporation is neglected. Here,  $\Delta z$  corresponds to the distance between the pressure tap at the inlet and outlet of the test section.

$$\left( \frac{\Delta p}{\Delta z} \right)_{\text{acc,h}} = \dot{m}_0^2 \cdot \left( \frac{1}{\rho_V} - \frac{1}{\rho_L} \right) \cdot \frac{\Delta \dot{x}}{\Delta z} \quad (\text{B.1})$$

$$\left( \frac{\Delta p}{\Delta z} \right)_{\text{acc,D}} = \dot{m}_0^2 \cdot \left[ \frac{\dot{x}^2}{\varepsilon \cdot \rho_V} + \frac{(1 - \dot{x})^2}{(1 - \varepsilon) \cdot \rho_L} \right]_{\text{inlet}}^{\text{outlet}} \cdot \frac{1}{\Delta z} \quad (\text{B.2})$$

**Incompressibility of the vapor phase:**

Following the approach of Weise et al. [22] the vapor phase can be assumed incompressible if the Mach number  $Ma$  meets the criterion shown in Eq. (B.3). Thereby, the vapor is treated as an ideal gas. The isobaric and isochoric specific heat capacity are  $c_p$  and  $c_v$ .

$$Ma = \frac{\dot{m}_0}{\psi_o} \ll \sqrt{\frac{1}{\dot{x}}} \quad (\text{B.3})$$

$$\sqrt{\frac{c_v}{c_p} \cdot p \cdot \rho_V}$$

**Equivalent particle Reynolds number:**

To approximate the flow regime in POCS with cubic cell geometries (cu, n-cu), Klumpp et al. [15] used the equivalent particle Reynolds number  $Re_p$  according to Eq. (B.4). As the characteristic length scale, they used the equivalent particle diameter  $d_p$  (see Eq. (B.5)).

$$Re_p = \frac{u_0 \cdot d_p \cdot \rho_F}{\eta_F} \quad (\text{B.4})$$

$$d_p = \frac{6 \cdot (1 - \psi_o)}{S_V} \quad (\text{B.5})$$

## Appendix C

**Vapor quality:**

The vapor quality  $\dot{x}_k$  is determined with Eq. (C.1) by means of an enthalpy balance of the pre-evaporator and the test section. The control volume extends from the inlet of the pre-evaporators to the respective plane of measurement  $k$ .

$$\dot{x}_k = \frac{\sum \dot{Q} - (H_{L,k} - H_{L,\text{inl}}) \cdot \dot{M}}{\Delta H_{L,v,k} \cdot \dot{M}} \quad (\text{C.1})$$

The specific enthalpy of the subcooled  $\text{CO}_2$  at the pre-evaporator inlet  $H_{L,\text{inl}}$  and the specific enthalpy of evaporation at the respective plane of measurement  $\Delta H_{L,v,k}$  are determined as a function of the saturation pressure  $p_k$ . For a more detailed description, see [36].

**Dry angle:**

In [6] only the transition from distracted stratified to annular flow was found to be relevant for calculating the circumferentially averaged heat transfer coefficients. Therefore, no distinction is made between distracted stratified and intermittent flow in the calculation of the dry angle. As a result the total dry angle  $\theta_{\text{dry}}$  for distracted stratified flow is calculated according to the approach of Lu and Zhao [47,48] by a linear interpolation of the

annular and stratified flow transition curves (see Eq. (C.2)). In this regard, the transition curve to stratified flow was set to zero as it occurs at very low mass fluxes with porous inserts. The transition to annular flow respectively complete wetting of the circumference corresponds to the mass flux  $\dot{m}_{0,a}$ . Since porous inserts influence the wetting of the circumference dependent on their cell geometries no universally applicable flow pattern maps exist and  $\dot{m}_{0,a}$  has to be determined experimentally. The corresponding dry angle of a stratified flow in the empty tube  $\theta_{dry, st}$  is calculated with Eq. (C.3) according to Biberger [49].

$$\theta_{dry} = \frac{(\dot{m}_{0,a} - \dot{m}_0)}{\dot{m}_{0,a}} \cdot \theta_{dry, st} \quad (C.2)$$

$$\theta_{dry, st} = 2\pi - 2 \left\{ \left( \frac{3\pi}{2} \right)^{1/3} \cdot \left[ 1 - 2 \cdot (1 - \varepsilon) + (1 - \varepsilon)^{1/3} - \varepsilon^3 \right] + \pi \cdot (1 - \varepsilon) - \frac{(1 - \varepsilon) \cdot \varepsilon}{200} [1 - 2 \cdot (1 - \varepsilon)] \cdot [1 + 4 \cdot (1 - \varepsilon)^2 + \varepsilon^2] \right\} \quad (C.3)$$

Fig. C.1 shows a schematic depiction of the symmetrical distribution of the dry angle  $\theta_{dry}$  over circumference of the tube.

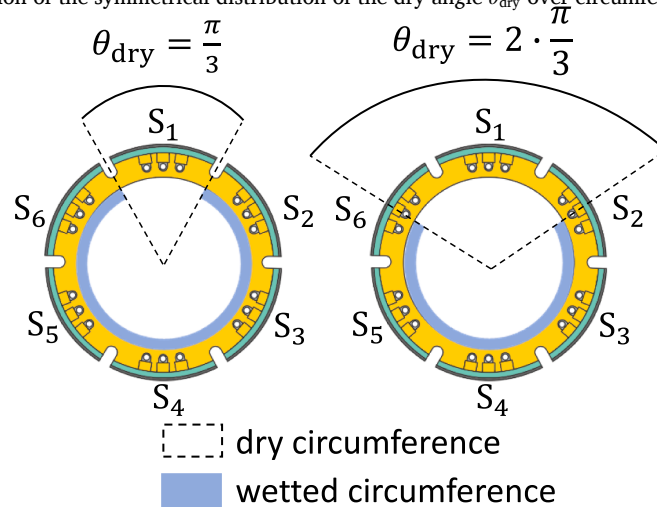


Fig. C.1. Schematic depiction of the symmetrical distribution of the dry angle  $\theta_{dry}$  over the circumference of the tube. Depiction was modified from Weise et al. [37] (licensed under CC BY-NC 4.0 DEED).

**Convective boiling model for empty tubes (Kattan et al. [2]):**

$$Nu_{cb} = \frac{h_{cb} \cdot \delta}{\lambda_L} = 0.0133 \cdot Re_L^{0.69} \cdot Pr_L^{0.4} \quad (C.4)$$

The Reynolds number  $Re_L$  is determined with Eq. (C.5) with the void fraction  $\varepsilon$  calculated according to the drift flux model of Rouhani [29] (see Section 2.1).

$$Re_L = \frac{4 \cdot \dot{m}_0 \cdot (1 - \dot{x}) \cdot \delta}{(1 - \varepsilon) \cdot \eta_L} \quad (C.5)$$

The film thickness  $\delta$  is calculated according to Eq. (C.6).

$$\delta = \frac{\pi \cdot d_i \cdot (1 - \varepsilon)}{2 \cdot (2\pi - \theta_{dry})} \quad (C.6)$$

## References

- [1] S. Weise, B. Dietrich, T. Wetzel, Flow-pattern based prediction of flow boiling heat transfer in horizontal tubes with circumferentially varying heat flux, *Int. J. Heat Mass Transf.* 148 (2020) 119018.
- [2] N. Kattan, D. Favrat, J. Thome, Flow boiling in horizontal tubes: part 1—development of a diabatic two-phase flow pattern map, *J. Heat Transf.* 120 (1998).
- [3] L. Wojtan, T. Ursenbacher, J.R. Thome, Investigation of flow boiling in horizontal tubes: part II—development of a new heat transfer model for stratified-wavy, dryout and mist flow regimes, *Int. J. Heat Mass Transf.* 48 (14) (2005) 2970–2985.
- [4] L. Cheng, G. Ribatski, J.R. Thome, New prediction methods for CO2 evaporation inside tubes: part II—an updated general flow boiling heat transfer model based on flow patterns, *Int. J. Heat Mass Transf.* 51 (1) (2008) 125–135.
- [5] R. Mastrullo, A.W. Mauro, J.R. Thome, D. Toto, G.P. Vanoli, Flow pattern maps for convective boiling of CO2 and R410A in a horizontal smooth tube: experiments and new correlations analyzing the effect of the reduced pressure, *Int. J. Heat Mass Transf.* 55 (5) (2012) 1519–1528.
- [6] S. Weise, T. Wetzel, B. Dietrich, Influence of porous inserts on flow boiling heat transfer in horizontal tubes, *Int. J. Heat Mass Transf.* 171 (2021) 121087.
- [7] G. Bamorovat Abadi, C. Moon, K.Chun Kim, Flow boiling visualization and heat transfer in metal-foam-filled mini tubes – Part I: flow pattern map and experimental data, *Int. J. Heat Mass Transf.* 98 (2016) 857–867.
- [8] Y. Zhu, H. Hu, S. Sun, G. Ding, Flow boiling of refrigerant in horizontal metal-foam filled tubes: part 2 – A flow-pattern based prediction method for heat transfer, *Int. J. Heat Mass Transf.* 91 (2015) 502–511.
- [9] C.Y. Zhao, W. Lu, S.A. Tassou, Flow boiling heat transfer in horizontal metal-foam tubes, *J. Heat Transf.* 131 (12) (2009).
- [10] P. Drögemüller, The use of hiTRAN wire matrix elements to improve the thermal efficiency of tubular heat exchangers in single and two-phase flow, *Chem. Ing. Tech.* 87 (3) (2015) 188–202.
- [11] C. Busse, H. Freund, W. Schwieger, Intensification of heat transfer in catalytic reactors by additively manufactured periodic open cellular structures (POCS), *Chem. Eng. Process. Process Intensif.* 124 (2018) 199–214.
- [12] C. Parra-Cabrera, C. Achille, S. Kuhn, R. Ameloot, 3D printing in chemical engineering and catalytic technology: structured catalysts, mixers and reactors, *Chem. Soc. Rev.* 47 (1) (2018) 209–230.
- [13] K. Dubil, H. Wolf, T. Wetzel, B. Dietrich, Development of a generalized thermal resistance model for the calculation of effective thermal conductivities in periodic open cellular structures (POCS), *Int. J. Heat Mass Transf.* 183 (2022) 122083.
- [14] C. Ferroni, M. Bracconi, M. Ambrosetti, M. Maestri, G. Groppi, E. Tronconi, A fundamental investigation of gas/solid heat and mass transfer in structured

- catalysts based on periodic open cellular structures (POCS), *Ind. Eng. Chem. Res.* 60 (29) (2021) 10522–10538.
- [15] M. Klumpp, A. Inayat, J. Schwerdtfeger, C. Körner, R.F. Singer, H. Freund, W. Schwieger, Periodic open cellular structures with ideal cubic cell geometry: effect of porosity and cell orientation on pressure drop behavior, *Chem. Eng. J.* 242 (2014) 364–378.
- [16] I. Kaur, P. Singh, Flow and thermal transport through unit cell topologies of cubic and octahedron families, *Int. J. Heat Mass Transf.* 158 (2020) 119784.
- [17] C. Hutter, D. Büchi, V. Zuber, P. Rudolf von Rohr, Heat transfer in metal foams and designed porous media, *Chem. Eng. Sci.* 66 (17) (2011) 3806–3814.
- [18] K. Dubil, T. Wetzel, B. Dietrich, Modelling steady-state convective heat transfer in different periodic open cellular structures (POCS) – A superposition approach, *Int. J. Heat Mass Transf.* 200 (2023) 123546.
- [19] M. Lämmermann, G. Horak, W. Schwieger, H. Freund, Periodic open cellular structures (POCS) for intensification of multiphase reactors: liquid holdup and two-phase pressure drop, *Chem. Eng. Process. Process Intensif.* 126 (2018) 178–189.
- [20] M. Lämmermann, W. Schwieger, H. Freund, Experimental investigation of gas-liquid distribution in periodic open cellular structures as potential catalyst supports, *Catal. Today* 273 (2016) 161–171.
- [21] C. Spille, A. Lyberis, M. Isabelle Maiwald, D. Herzog, M. Hoffmann, C. Emmelmann, M. Schlüter, SMART-reactors: tailoring gas holdup distribution by additively manufactured lattice structures, *Chem. Eng. Technol.* 43 (10) (2020) 2053–2061.
- [22] S. Weise, S. Meinicke, T. Wetzel, B. Dietrich, Modelling the pressure drop of two-phase flow through solid porous media, *Int. J. Multiph. Flow* 112 (2019) 13–26.
- [23] S.S. Bhatti, Environment-friendly refrigerants for sustainable refrigeration and air conditioning: a review, *Curr. World Environ.* 18 (3) (2023) 933–947.
- [24] M.A. Woldeamayrat, A.J. Ghajar, Comparison of void fraction correlations for different flow patterns in horizontal and upward inclined pipes, *Int. J. Multiph. Flow* 33 (4) (2007) 347–370.
- [25] J.R. Thome, A. Cioncolini, Chapter 6 - two-phase pressure drop, Thome J. R. (Ed.), *Encyclopedia of Two-Phase Heat Transfer and Flow I. Fundamentals and Methods*, World Scientific Publishing, New Jersey, 2015, pp. 143–176.
- [26] J.R. Thome, A. Cioncolini, Chapter 7 - the drift flux model, Thome J. R. (Ed.), *Encyclopedia of Two-Phase Heat Transfer and Flow I. Fundamentals and Methods*, World Scientific Publishing, New Jersey, 2015, pp. 185–194.
- [27] N. Zuber, J.A. Findlay, Average volumetric concentration in two-phase flow systems, *J. Heat Transf.* 87 (4) (1965) 453–468.
- [28] L. Wojtan, T. Ursenbacher, J.R. Thome, Investigation of flow boiling in horizontal tubes: part I—A new diabatic two-phase flow pattern map, *Int. J. Heat Mass Transf.* 48 (14) (2005) 2955–2969.
- [29] S.Z. Rouhani, Modified correlations for void and two-phase pressure drop, *AE-RTV* 841. Hg. v. AB Atomenergi Sweden (1969).
- [30] A. Diani, S. Mancin, L. Doretto, L. Rossetto, Low-GWP refrigerants flow boiling heat transfer in a 5 PPI copper foam, *Int. J. Multiph. Flow* 76 (2015) 111–121.
- [31] E. Skjetne, J.L. Auriault, New insights on steady, non-linear flow in porous media, *Eur. J. Mech. B Fluids* 18 (1) (1999) 131–145.
- [32] D.L. Koch, A.J.C. Ladd, Moderate Reynolds number flows through periodic and random arrays of aligned cylinders, *J. Fluid Mech.* 349 (1997) 31–66.
- [33] A. Inayat, M. Klumpp, M. von Beyer, H. Freund, W. Schwieger, Development of a new pressure drop correlation for open-cell foams based completely on theoretical grounds: taking into account strut shape and geometric tortuosity, *Chem. Eng. J.* 287 (2016) 704–719.
- [34] E. Bianchi, G. Groppi, W. Schwieger, E. Tronconi, H. Freund, Numerical simulation of heat transfer in the near-wall region of tubular reactors packed with metal open-cell foams, *Chem. Eng. J.* 264 (2015) 268–279.
- [35] M.G. Cooper, Saturation nucleate pool boiling - A simple correlation, in: *First U.K. National Conference on Heat Transfer*, 2 (1984), 785–793, Leeds.
- [36] S.M. Haertlé, Flow boiling of CO<sub>2</sub> in porous structures. Ph.D. thesis, Karlsruher Institut für Technologie (KIT), 2023.
- [37] S. Weise, S. Klein, R. Orias Calvo, F. Müller-Trefzer, T. Wetzel, B. Dietrich, Heat transfer data of two-phase flow in a horizontal tube filled with metal sponge, KITopen repository (2019).
- [38] BIPM, IEC, IFCC, ILAC, ISO, IUPAC, IUPAP, and OIML, Evaluation of measurement data - guide to the expression of uncertainty in measurement. Joint Committee for Guides in Metrology, JCGM 100:2008, URL: [https://www.bipm.org/documents/20126/2071204/JCGM\\_100\\_2008\\_E.pdf/](https://www.bipm.org/documents/20126/2071204/JCGM_100_2008_E.pdf/), Retrieved November 2023.
- [39] R. Span, W. Wagner, A new equation of state for carbon dioxide covering the fluid region from the triple-point temperature to 1100 K at Pressures up to 800 MPa, *J. Phys. Chem. Ref. Data* 25 (6) (1996) 1509–1596.
- [40] T.J. Horneber, Thermo-fluid dynamic characterization and technical optimization of structured open-cell metal foams by means of numerical simulation (2015), Dissertation, Der Technischen Fakultät der Friedrich-Alexander-Universität Erlangen-Nürnberg.
- [41] I.R. Woodward, L.M. Attia, P. Patel, C.A. Fromen, Scalable 3D-printed lattices for pressure control in fluid applications, *AIChE J.* 67 (12) (2021).
- [42] S. Meinicke, Understanding transport phenomena in highly porous media - a pore scale CFD approach (2019), Dissertation. 1. Auflage. München: Verlag Dr. Hut.
- [43] A. Duda, Z. Koza, M. Matyka, Hydraulic tortuosity in arbitrary porous media flow, *Phys. Rev. E* 84 (3) (2011) 36319.
- [44] MatWeb Material property data, 3D systems laserforms AlSi10Mg (A), Direct aging aluminum alloy material, <https://www.matweb.com/search/datasheet.aspx?matguid=9c8a7903a137449b88e11ed9743edd10>, Retrieved November 2023.
- [45] M. Nirish, R. Rajendra, Optimization process parameter on wear characterization of Al6061 and AlSi10Mg Alloy manufactured by selective laser melting, *J. 3D Print. Addit. Manuf.* 1 (2022).
- [46] H.M. Müller, D. Steiner, Druckverlust bei der Strömung von Argon und Stickstoff in einem horizontalen Verdampferrohr, Kraußold H. und Schlünder U. (Ed.). *Vt - Verfahrenstechnik*. 17. Jahrgang. Zeitschrift für den Ingenieur in Entwicklung, Planung und Produktion, Organ der Fachgemeinschaft Apparatebau im VDMA, Krausskopf, Mainz, 1983, pp. 519–523.
- [47] W. Lu, Investigation of Heat Transfer in Metal-Foam Tubes, Brunel University School of Engineering and Design, 2008. PhD Theses.
- [48] W. Lu, C.Y. Zhao, Numerical modelling of flow boiling heat transfer in horizontal metal-foam tubes, *Adv. Eng. Mater.* 11 (10) (2009) 832–836.
- [49] D. Biberger, An explicit approximation for the wetted angle in two-Phase stratified pipe flow, *Can. J. Chem. Eng.* 77 (6) (1999) 1221–1224.